

HST/WFPC2 OBSERVATIONS OF WARM ULTRALUMINOUS INFRARED GALAXIES¹

JASON A. SURACE, D. B. SANDERS, AND WILLIAM D. VACCA

University of Hawaii, Institute for Astronomy, 2680 Woodlawn Drive, Honolulu, HI 96822;
 jason@ifa.hawaii.edu, sanders@ifa.hawaii.edu, vacca@ifa.hawaii.edu

SYLVAIN VILLEUX

University of Maryland, Department of Astronomy, College Park, MD 20742; villeux@astro.umd.edu

AND

J. M. MAZZARELLA

Infrared Processing and Analysis Center, M/S 100-22, 770 South Wilson Avenue, California Institute of Technology,
 Jet Propulsion Laboratory, Pasadena, CA 91125; mazz@ipac.caltech.edu

Received 1997 May 5; accepted 1997 August 13

ABSTRACT

We present new high-resolution *B*- and *I*-band images of a nearly complete sample of nine “warm” ($f_{25}/f_{60} > 0.2$), ultraluminous infrared galaxies (ULIGs) obtained with the Wide Field Planetary Camera of the *Hubble Space Telescope* (*HST*). The *HST* images clearly reveal the presence of tidal tails and other features associated with merging galaxies. All of the warm ULIGs show evidence of complex structures such as dust lanes and spiral features in their inner few kiloparsecs. Additionally, they show compact, blue “knots” of star formation (between 4 and 31 knots per object) that appear similar to those seen in more nearby merger systems. Spectral synthesis modeling is used to estimate mean upper age limits and masses: the median upper age limit for the knots in individual galaxies is $\sim 3 \times 10^8$ yr (ranging from $\sim 10^7$ to 1×10^9 yr), and the range of knot masses is $\sim 10^5$ – $10^9 M_{\odot}$. We also argue that these starburst knots cannot be significant contributors to the extremely high bolometric luminosity of these galaxies. Additionally, each object contains one or two knots whose luminosity and color are implausible in terms of star formation; we identify these as putative active nuclei. These observations are consistent with the hypothesis that warm ULIGs may represent a critical transition stage in the evolution of ULIGs into optical quasi-stellar objects.

Subject headings: galaxies: active — galaxies: interactions — galaxies: starburst — galaxies: star clusters — infrared: galaxies

1. INTRODUCTION

One of the most important results of the *IRAS*² all-sky survey was the discovery of a significant population of galaxies that emit the bulk of their luminosity in the far-infrared (e.g., Soifer et al. 1984). Studies of the properties of these “infrared” galaxies show systematic trends coupled to the total far-infrared luminosity; more luminous systems were more likely to appear to be merger remnants or interacting pairs, and they were more likely to possess active galactic nucleus-like emission-line features. A more complete review of the properties of luminous infrared galaxies can be found in Sanders & Mirabel (1996). Much recent attention has been focused on ultraluminous infrared galaxies (ULIGs), objects with infrared luminosities, L_{ir} ,³ greater than $10^{12} L_{\odot}$, which corresponds to the bolometric luminosity of quasi-stellar objects (QSOs) (i.e., $M_{\text{B}} < -22.1$; Schmidt & Green 1983). Multiwavelength observations of a complete sample of 10 ULIGs led Sanders et al.

(1988b) to suggest that these objects might plausibly represent the initial dust-enshrouded stage in the evolution of optically selected QSOs, and that the majority, if not all QSOs, may begin their lives in such an intense infrared phase.

An important subset of ULIGs are those objects with “warm” ($f_{25}/f_{60} > 0.2$),⁴ mid-infrared colors. These warm objects, which represent $\sim 20\%$ – 25% of the total population of ULIGs, appear to represent a critical transition stage in the evolution of the larger population of “cool” ULIGs into optical QSOs. Studies of several small but complete samples of warm ULIGs have shown that many of these objects have a pointlike optical appearance on the Palomar Sky Survey and that they exhibit broad (Seyfert 1) optical emission lines, characteristics that have led them to be referred to as “infrared QSOs” (e.g., Low et al. 1988; Sanders et al. 1988c). The complete flux-limited sample of 12 warm ULIGs from the survey of Sanders et al. (1988c) has been particularly useful for study. As the nearest and brightest warm ULIGs, these objects are the most amenable to studies at other wavelengths.

This paper presents the first *Hubble Space Telescope* (*HST*) images obtained with the Wide Field Planetary Camera (WFPC2) of the majority of the warm ULIGs in the sample of Sanders et al. (1988c). The sample, observations, and data reduction techniques are described in §§ 2,

¹ Based on observations with the NASA/ESA *Hubble Space Telescope*, obtained at the Space Telescope Science Institute, which is operated by the Association of Universities for Research in Astronomy, Inc., under NASA contract NAS 5-26555.

² The *Infrared Astronomical Satellite* was developed and operated by the US National Aeronautics and Space Administration (NASA), the Netherlands Agency for Aerospace Programs (NIVR), and the UK Science and Engineering Research Council (SERC).

³ $L_{\text{ir}} \equiv L(8\text{--}1000 \mu\text{m})$ is computed using the flux in all four *IRAS* bands according to the prescription given in Perault (1987; see also Sanders & Mirabel 1996). Throughout this paper, we use $H_0 = 75 \text{ km s}^{-1} \text{ Mpc}^{-1}$ and $q_0 = 0.5$ (unless otherwise noted).

⁴ The quantities f_{12} , f_{25} , f_{60} , and f_{100} represent the *IRAS* flux densities (non-color-corrected) in units of jansky at 12, 25, 60, and 100 μm , respectively.

TABLE 1
WARM ULIGs OBSERVED BY *HST*

Name	R.A. (J2000.0)	Decl. (J2000.0)	z	$\log(L_{\text{ir}}/L_{\odot})$	$\log(L_{\text{bol}}/L_{\odot})$	F439W (s)	F814W (s)
IRAS 01003–2238.....	01 02 49.83	–22 21 56.3	0.118	12.22	12.28	3030	1100
Mrk 1014	01 59 50.8	00 23 41.5	0.163	12.50	12.80	1380	480
IRAS 05189–2524.....	05 21 01.53	–25 21 46.7	0.042	12.08	12.17	2830	1313
IRAS 08572+3915.....	09 00 25.42	39 03 54.2	0.058	12.10	12.19	2830	1320
IRAS 12071–0444.....	12 09 45.10	–05 01 13.7	0.129	12.32	12.38	2500	1200
Mrk 231.....	12 56 14.24	56 52 26.1	0.042	12.52	12.67	2226	712
PKS 1345+12.....	13 47 33.55	12 17 24.5	0.122	12.25	12.41	2700	985
Mrk 463.....	13 56 02.74	18 22 18.3	0.051	11.77	12.03	1030	360
IRAS 15206+3342.....	15 22 37.96	33 31 36.6	0.125	12.16	12.24	3000	1030

NOTE.—The names are as given in Sanders et al. 1988c, with new astrometric positions derived from the STScI Digital Sky Survey. Units of right ascension are hours, minutes, and seconds, and units of declination are degrees, arcminutes, and arcseconds. Redshift and L_{ir} are from Kim & Sanders 1997, with additional luminosity needed to compute L_{bol} taken from Sanders et al. 1988c.

3, and 4, respectively. In § 5, we present the main results, including descriptions of the large-scale morphology and colors revealed by the new *HST* images, and the somewhat surprising discovery of a large population of extremely

luminous “knots” that appear to be a common feature of all warm ULIGs. In § 6, we discuss the properties of these knots in terms of starburst models and, in addition, identify one or two putative nuclei in each object. Both the large-

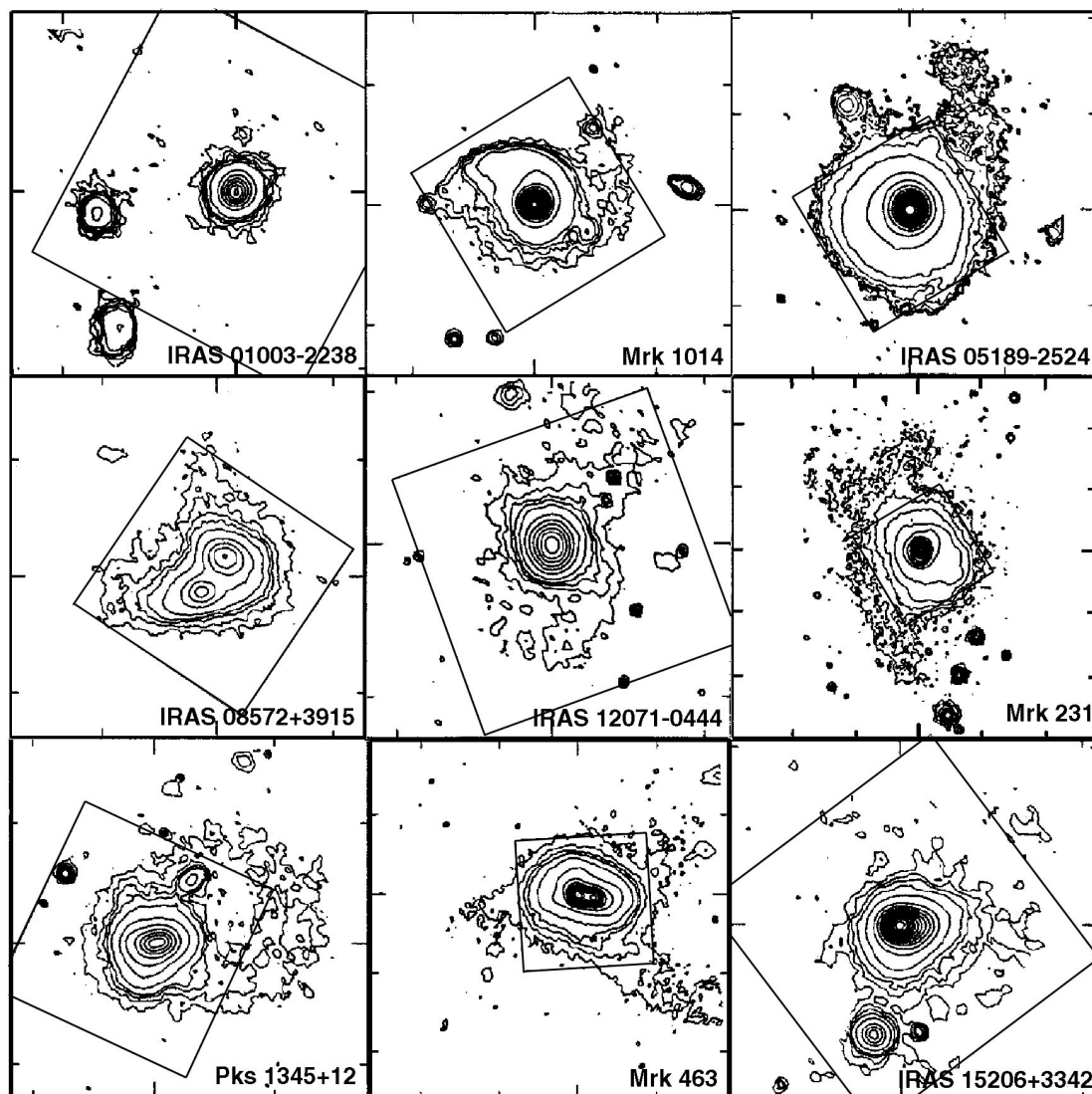


FIG. 1.—The PC FOV ($36'' \times 36''$) superimposed on contour maps of the ground-based Gunn r images of the nine warm ULIGs. The ground-based data are from Sanders et al. (1988c). The galaxies are ordered by increasing right ascension, from left to right, top to bottom. All images are displayed with north at the top and east to the left.

scale structure and the knot properties of warm ULIGs are then compared with features that have been detected recently in *HST* images of nearby optically selected QSOs.

2. SAMPLE

Of the 12 warm ULIGs in our complete sample, nine were observed with *HST* in our cycle 5 GO program, the remaining three sources having already been included in previously approved GTO and/or GO programs: 3C 273 (various cycles; Bahcall, Kirkhakos, & Schneider 1995), IRAS 07598 + 6508 (cycle 5; Boyce et al. 1996), and I Zw 1 (several GO programs in cycles 3–5). The nine targets observed by us are listed in Table 1 along with the target coordinates, redshift, infrared and bolometric luminosity, and the *HST* exposure times.

An initial description of the properties of the complete sample as determined from ground-based studies—including optical morphology, optical spectral type, and the radio-to-UV spectral energy distribution (SED)—was presented in Sanders et al. (1988c). Three of the 12 warm ULIGs (I Zw 1, Mrk 1014, and 3C 273) were previously classified as optical QSOs, while the remainder are type 1 or 2 Seyfert galaxies. Six of the 12 objects have a dominant pointlike optical nucleus on the Palomar Sky Survey plates, similar in appearance to optically selected QSOs. Deep ground-based optical images show that three of the 12 have double nuclei while most of the remaining objects exhibit large-scale tidal features characteristic of advanced mergers. A more complete description of each of the nine objects observed by us and the remaining three observed by others with *HST* is given in the Appendix. Ground-based images are also shown in Figure 1.

Since all of the warm ULIGs in our sample are at redshifts 0.05–0.15, the physical resolution that is optically achievable from the ground is only about 1–2 kpc, which is clearly insufficient to disentangle such structures as nuclear bars or rings that, for example, might be associated with a circumnuclear starburst, or to disentangle the relative contributions of such a starburst from any active galactic nucleus (AGN) component that might be present. The higher resolution of *HST* also permits much more accurate photometry, allowing, for example, a more detailed examination of stellar populations. Finally, the low background in space, accompanied by the increase in point-source detectability due to higher spatial resolution, enables us to search for very faint high spatial frequency structure.

3. OBSERVATIONS

The *HST* data were taken in cycle 5 between 1995 September and 1996 March with the WFPC2 camera. In all cases, the apparent optical nucleus of the target was centered on the PC chip at the position listed in Table 1. The PC was chosen for its superior spatial sampling ($0''.046 \text{ pixel}^{-1}$) compared with the WF camera. The PC field of view (FOV) is shown in Figure 1 superimposed on deep ground-based images of each target. In most cases, all of the detectable structure fell within the $36''$ FOV of the PC, although in the case of Mrk 231 and IRAS 05189–2524 some additional structure was detected in the flanking WF fields. Because of the nonsymmetric orientation of the WF fields in relation to the PC, the random rotation angle introduced by the spacecraft, and the geometry of the galaxies, it was not possible in all cases to arrange to observe the inner

galaxy with the PC and, simultaneously, to capture the full extent of the outer disk and large-scale tidal features with the WF fields. In any case, as shown by the PC data, the outer regions of these galaxies are of too low a surface brightness to be imaged with WFPC2 without much longer integration times.

For each galaxy, exposures were made using the F439W and F814W filters, which correspond closely to the standard Johnson *B* and Cousins *I* filters (see Holtzman et al. 1995a, 1995b). In the remainder of this paper, we refer to these filters simply as *B* and *I*. In each filter, one short exposure was made to image any bright features without saturation, and then the remaining time was split into two or three long exposures in order to identify cosmic rays. The ratio of exposure times in the *B* and *I* filters was approximately 3:1 (see Table 1) in an attempt to ensure a similar signal-to-noise ratio (S/N) at both wavelengths, although scheduling constraints often necessitated somewhat varying times. In general, each target was observed during one or two consecutive orbits, with a time interval of several weeks between targets.

4. DATA REDUCTION

Dark subtraction, bias subtraction, and flat-fielding were carried out using the standard data reduction pipeline procedures at STScI. The spacecraft was commanded to keep the field in a fixed position and orientation throughout the observations, eliminating the need for later registration. This was confirmed by examining the location of the centroids of the nuclei, the stars in the frame, and the extended structure. The image rotation introduced by the roll angle of the spacecraft was removed by rotating the image using linear interpolation according to the amount specified by STScI based on spacecraft telemetry. All photometric analysis was carried out on the unrotated images in order to avoid the small uncertainties introduced by the rotation process. Images were combined using the IRAF/STSDAS routine GCOMBINE, which includes an algorithm for removal of cosmic rays from individual frames (effectively filling them in with good pixels from other frames). Saturated pixels in the bright nuclei were similarly replaced with data from the short exposures. The remaining bad pixels were identified by eye and by fabrication of comparison images constructed from only the lowest valued pixels in an image stack. These pixels were filled in by linear interpolation from surrounding pixels.

For each galaxy, additional observations were made of nearby stars within several arcminutes in order to accurately determine the point-spread function (PSF). In some cases, this was not entirely successful because of their low brightness in the *B* and *I* filters (since no previous observations in our filters existed, and their spectral types were unknown). Therefore, these observations were supplemented with models of the PSF made using the Tiny TIM software available from STScI (Krist 1994). Because of the PC undersampling and the considerable pixel-to-pixel scattering within the PC CCD, the actual PSF is somewhat variant depending on the exact location of the peak within a given pixel. Ten-times-oversampled models of the point-spread function were generated, and then shifted and rebinned to the actual data resolution and convolved with the pixel-pixel scattering function in order to derive a more accurate PSF model (Krist 1994). In most cases, it was found that the observed PSF, while qualitatively very

similar to the TIM model, had some significant deviations at the 10%–15% level, which seemed to vary from target to target. In general, the resolution and strehl ratio predicted by TIM was higher than actually observed.

Photometric calibration was performed using published photometric solutions for WFPC2 and the F439W and F814W filters. Corrections were made for charge transfer efficiency (Whitmore 1996), aperture size (Table 2a of Holtzman et al. 1995a), and detector gain (Holtzman et al. 1995b). Zero points and color corrections for conversion from the *HST* flight filter system to ground-based Johnson filters were taken from Table 7 of Holtzman et al. (1995b) and checked against those of Whitmore (1996). The derived magnitudes have an uncertainty associated with calibration of approximately 4%. Absolute magnitudes were derived from the expression

$$M' = m - 15.62 - 5 \log cz + 1.086(q_0 - 1)z, \quad (1)$$

which is correct for $H_0 = 75 \text{ km s}^{-1}$ and c in units of km s^{-1} (Peebles 1993). At these low redshifts, the choice of cosmology is relatively unimportant. M' is used to indicate that this expression corrects only for distance and does not include K -corrections (bandpass stretching and spectral dependence) or corrections for reddening. The most distant target is at redshift $z = 0.16$, and the median redshift for the sample is only $z = 0.09$; thus, K -corrections are likely to be quite small. Based on stellar synthesis models that are believed to be representative of some of the components described below, theoretical K -corrections were computed and were indeed found to be generally very small, typically $\Delta m = 0.1$ in the B and I filters at $z = 0.16$ for systems 10^7 – 10^8 years old, with extremes of $\Delta m = 0.4$ for extremely blue or red systems. K -corrections are not believed to affect derived colors by more than $\Delta(B-I) = 0.4$. Finally, since no actual observational SEDs exist for the features in these objects, it was felt that the uncertainties in assigning K -corrections probably outweighed any real benefit.

More importantly, no reddening corrections have been made to any magnitudes reported in this paper. The reddening in some regions of these galaxies may be quite large; Kim (1995) reports typical extinctions based on optical spectroscopy of $A_V = 2$ – 6 mag for the central ($2''$) regions of these systems, and $A_V = 4.5$ mag for Seyfert-like ULIGs in general. The effects of reddening are discussed more thoroughly in § 6.2.

5. RESULTS

5.1. Large-Scale Morphology and Colors

Figure 2 displays the large-scale structure seen in the PC observations of each of the observed ULIGs. Of the nine ULIGs, all except IRAS 01003–2238 show clear signs of recent merger activity in the form of tidal tails and loops. Additionally, IRAS 08572+3915, PKS 1345+12, and Mrk 463 have clear double nuclei. Further details can be seen in the near-true-color image of Figure 3 (Plate 1) for each of the nine objects. Figures 4 and 5 show close-ups of the individual nuclear regions in each ULIG (the small boxes in Fig. 2) at B and I , respectively. Most of the ULIGs show evidence of structure in the form of filaments, knots, and fans in their inner few kiloparsecs. Also, the *HST* images show evidence for small spatial scale features in the more extended structures that were previously observed from the ground (e.g., tidal tails). In the Appendix, we discuss these

features on an individual galaxy basis and their connection to previous ground-based images.

Figure 6 shows color maps ($B-I$) constructed by dividing the images for each object as shown in Figures 4 and 5. The effect of the wavelength-variant PSF on the derived colors was examined. Normally, the higher resolution at B would lead to color maps with excessively blue point sources; however, it appears that this is not actually a significant effect for these data. Color maps were constructed for the observed PSF stars that show a uniform color across the star's entire profile. Stars visible in the actual data frames were also used to confirm that the PSFs were well matched, although, in a few cases, convolution with a narrow Gaussian was needed to broaden the B profile in order to remove this color gradient more completely. Although PSF mismatch must be present to some degree in all the color maps, it appears to be small compared with the pixel-to-pixel variation in the color maps due to noise in the original images and blurring due to pixel-pixel scattering within the CCDs. Major distortions of the color map, which are due to PSF structure, are seen only in Mrk 1014 and Mrk 231, which are dominated by very bright point sources and therefore have very high S/N, even at the first diffraction ring.

Since low S/N regions in the B and I images result in very noisy color map regions, the color maps have been masked such that only regions with a $S/N \geq 5$ are displayed. As a result, very red regions are not displayed in the color maps since the S/N of the B images is usually lower than those at I . This effect can be seen in IRAS 08572+3915 (NW) and IRAS 15206+3342, where some regions become increasingly red and are then masked off. In these masked regions, $B-I$ is at least 3.

IRAS 01003–2238, Mrk 1014, and PKS 1345+12 have a reasonably simple color structure, perhaps indicating the presence of a uniform (if any) dust screen. The other six galaxies have a variety of different features. This varies from organized structures like the face-on spiral pattern of Mrk 231 and the dust lane that seems to bisect IRAS 05189–2524 to the rather chaotic pattern seen in IRAS 12071–0444 and the northwest nucleus of IRAS 08572+3915. Typical colors for spiral galaxies are $B-I = 1.8$ (Lu et al. 1993). As expected, in most cases the detectable background light in these galaxies is similar to this value. It is also apparent from the color maps that many of the ULIGs (notably Mrk 231, Mrk 463, and IRAS 15206+3342) show evidence of large numbers of blue ($B-I \leq 1.0$) pointlike features.

5.2. Knots

In each of the galaxies, we have identified bright compact regions that are usually bluer than the underlying galaxy and appear similar to the bright blue knots found in other interacting galaxies (e.g., NGC 4038/9; Whitmore & Schweizer 1995). These knots were identified on the basis of their peak surface brightness being 3 or more times the local background in either filter and being roughly circular, with closed isophotal contours (thereby differentiating them from the tidal streamers seen in some systems like Mrk 231 and IRAS 12071–0444). While three of the observed galaxies (Mrk 1014, IRAS 05189–2524, and PKS 1345+12) seem to have very few of these “knots,” the remaining six have as many as 30 each (in the cases of Mrk 231 and Mrk 463). The mean number of knots per galaxy is 13. Their

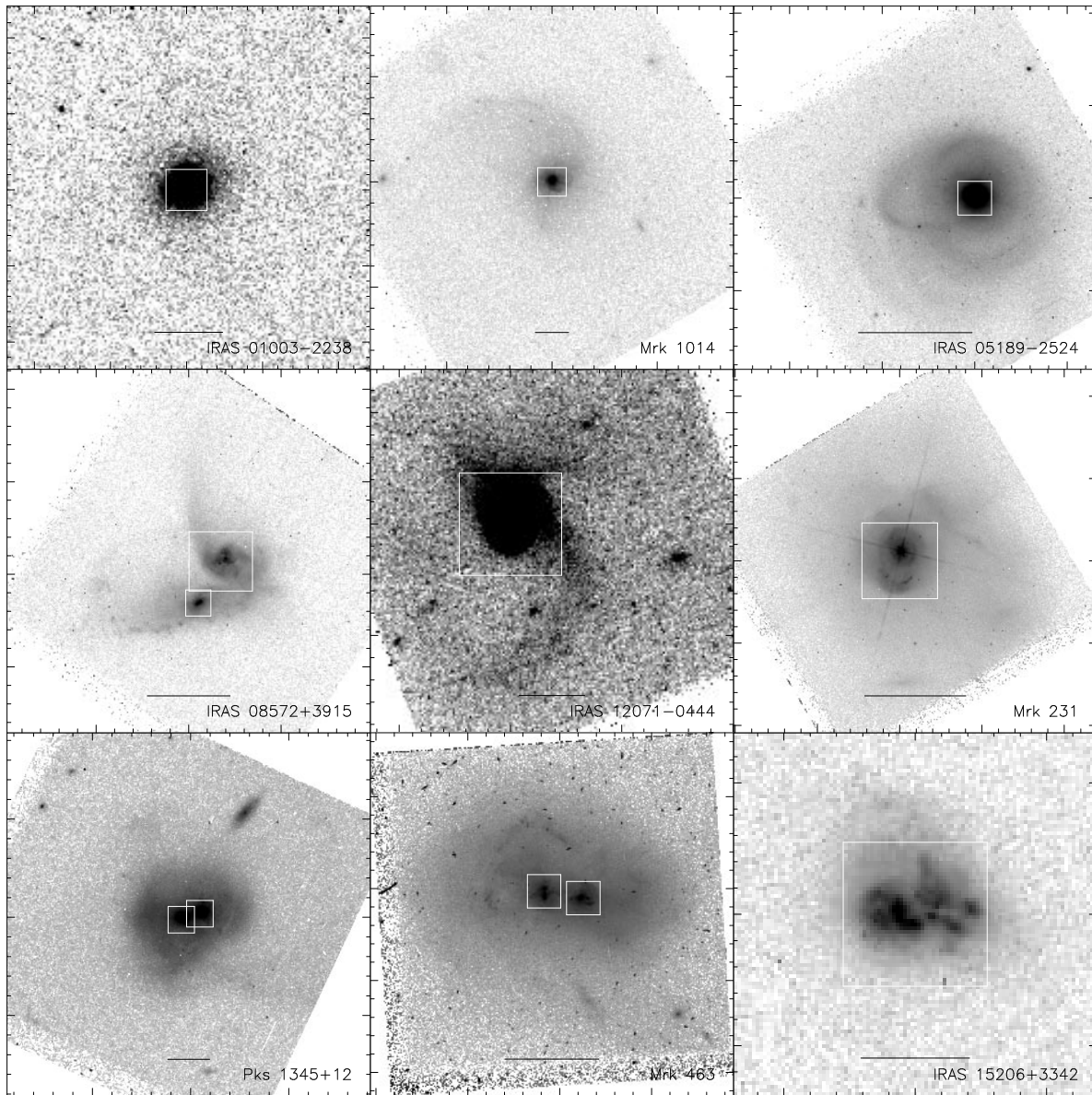


FIG. 2.—Large-scale structure of the nine warm ULIGs observed with the PC in the I band (F814W). In order to emphasize both faint and bright features, all images are block-averaged (3×3) and displayed with a nonlinear stretch. Major ticks are $10''$, except for IRAS 01003–2238 and IRAS 15206+3342, where each major tick is $5''$. The scale bar represents 10 kpc. The white boxes indicate the individual nuclear regions that will be displayed in Figs. 4–6.

locations are illustrated in Figure 7 and given in Table 2. For those systems with many knots, approximately half lie within 2 kpc of what appear to be nuclei (see § 5.3), while the remainder are spread along what appear to be inner tidal features (e.g., IRAS 08572+3915 and Mrk 463). The knots often appear to be arranged in linear structures or “strings” 1 or 2 knot widths wide and 4–5 knots long (the best examples can be found in IRAS 01003–2238, IRAS 12071–0444, Mrk 231, and IRAS 15206+3342).

The apparent magnitudes were measured for each of the identified knots. Initially, we attempted to derive fluxes by fitting them with the observed PSF. However, the uncertainties associated with this technique were very large (typically 1 mag). This was primarily true for the following reason: the marginal sampling of the PC, especially at B , made it difficult to constrain the fitted PSFs. Additionally, many of the knots appear to be slightly resolved, which renders this technique inappropriate. Magnitudes were

therefore derived from aperture photometry. Most of the photometry was derived from circular apertures typically 4–7 pixels in radius, although in some cases the irregular shape of the knots necessitated the use of polygonal apertures. These apertures varied in size, depending on the knot brightness, but were always made large enough (> 10 times the width of the PSF) so that aperture corrections for point sources tended to be fairly small. Additional aperture corrections due to the extended nature of the knots were computed after the knot sizes were measured (see below), although these corrections were generally small. Estimates were made of the underlying background galaxy flux by using the mean of the pixels in a 3-pixel annulus immediately outside the photometric aperture. In some cases, sections of the annuli had to be deleted owing to confusion with nearby structure. Most of the knots are isolated from one another by greater than 7 pixels, and hence confusion does not seem to be a serious problem (with the exception of

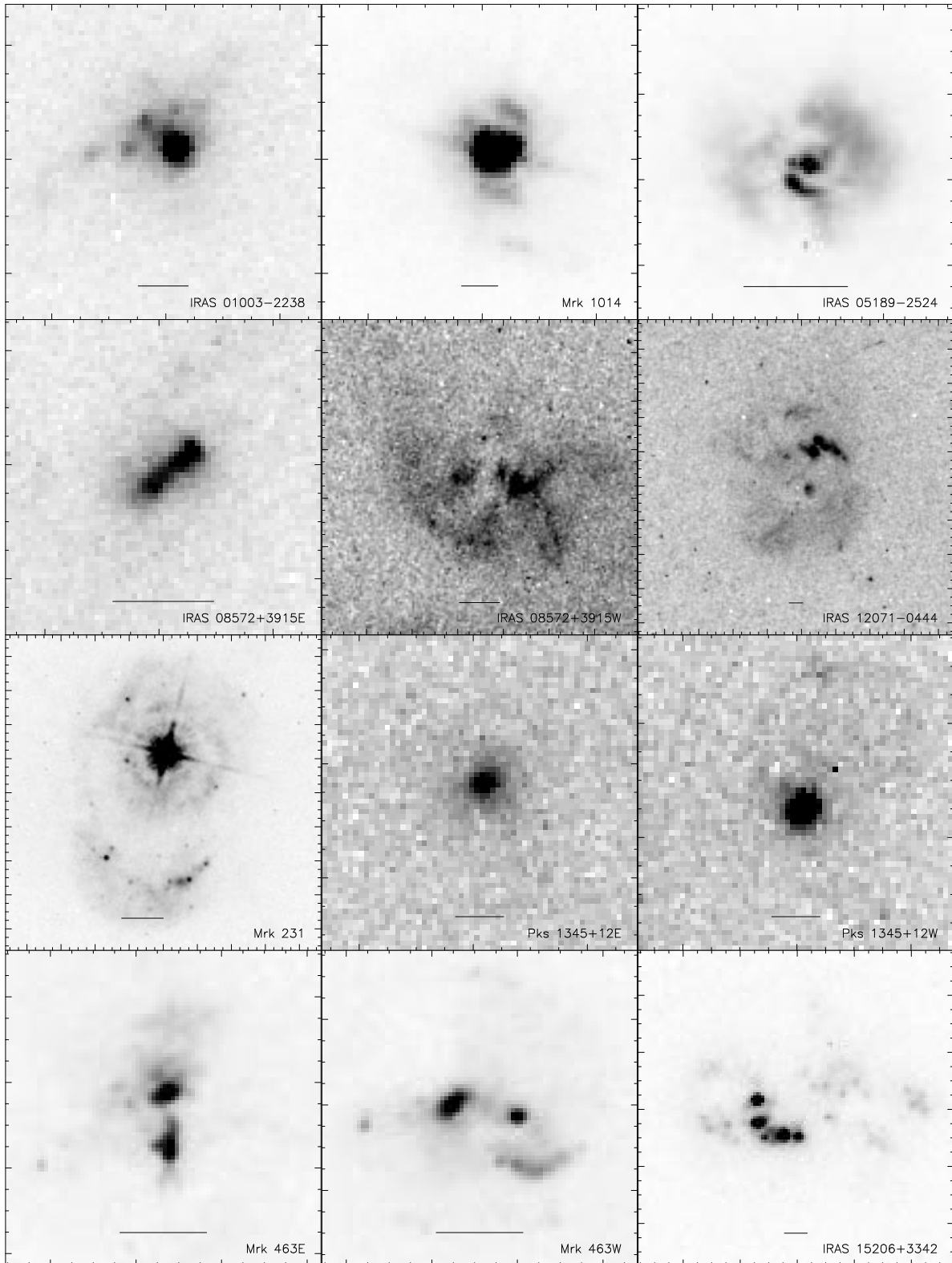


FIG. 4.—Close-up view of the nuclear regions of the warm ULIGs at the *B* band (F439W). The double nuclei in IRAS 08572+3915, PKS 1345+12, and Mrk 463 are displayed in separate panels labeled E (east) and W (west). The FOV represented by each of the 12 panels for the nine warm ULIGs is identical to the overlay boxes displayed in Fig. 2. The major ticks are in arcseconds, and the scale bar represents 1 kpc.

IRAS 15206+3342). The measured magnitudes for each of the knots, after correction for the background and aperture effects, are given in Table 2.

Simulations were performed in order to estimate the uncertainty of the measured fluxes. The observed point-

spread function was rescaled to the range of observed knot magnitudes and then added into various regions of the actual data for Mrk 231 and IRAS 05189-2524. Poisson noise and the effects of the detector gain and readout were all modeled using the parameters given for the PC in the

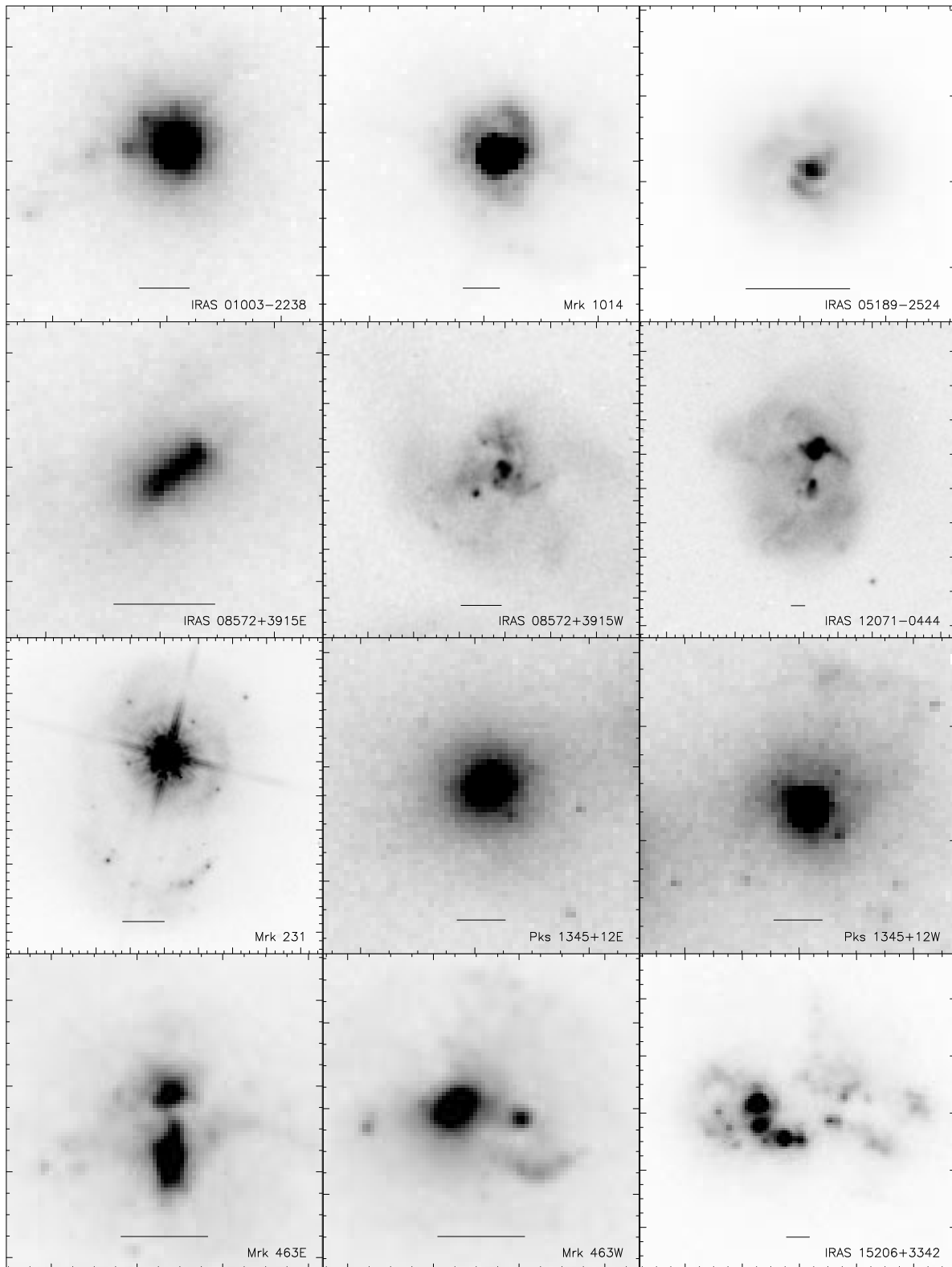


FIG. 5.—Close-up view of the nuclear regions of the warm ULIGs at the *I* band (F814W). The layout is the same as in Fig. 4.

WFPC2 instrument handbook. In this way, the uncertainty in point fluxes derived from real-data conditions, with fully simulated noise and confusion, could be examined. Attempts were then made to recover the known flux using the described aperture photometry technique. It was found that the magnitudes derived in this fashion had an associ-

ated uncertainty of about 0.25 between 24 and 26 mag, and decreased to about 0.05 mag at 23 mag and brighter. This is similar to the expected result based on the image noise statistics. Since most of the knots fall in the magnitude range from 22 to 26 (the 3σ limiting magnitude based on image noise statistics is generally between 26 and 27), a

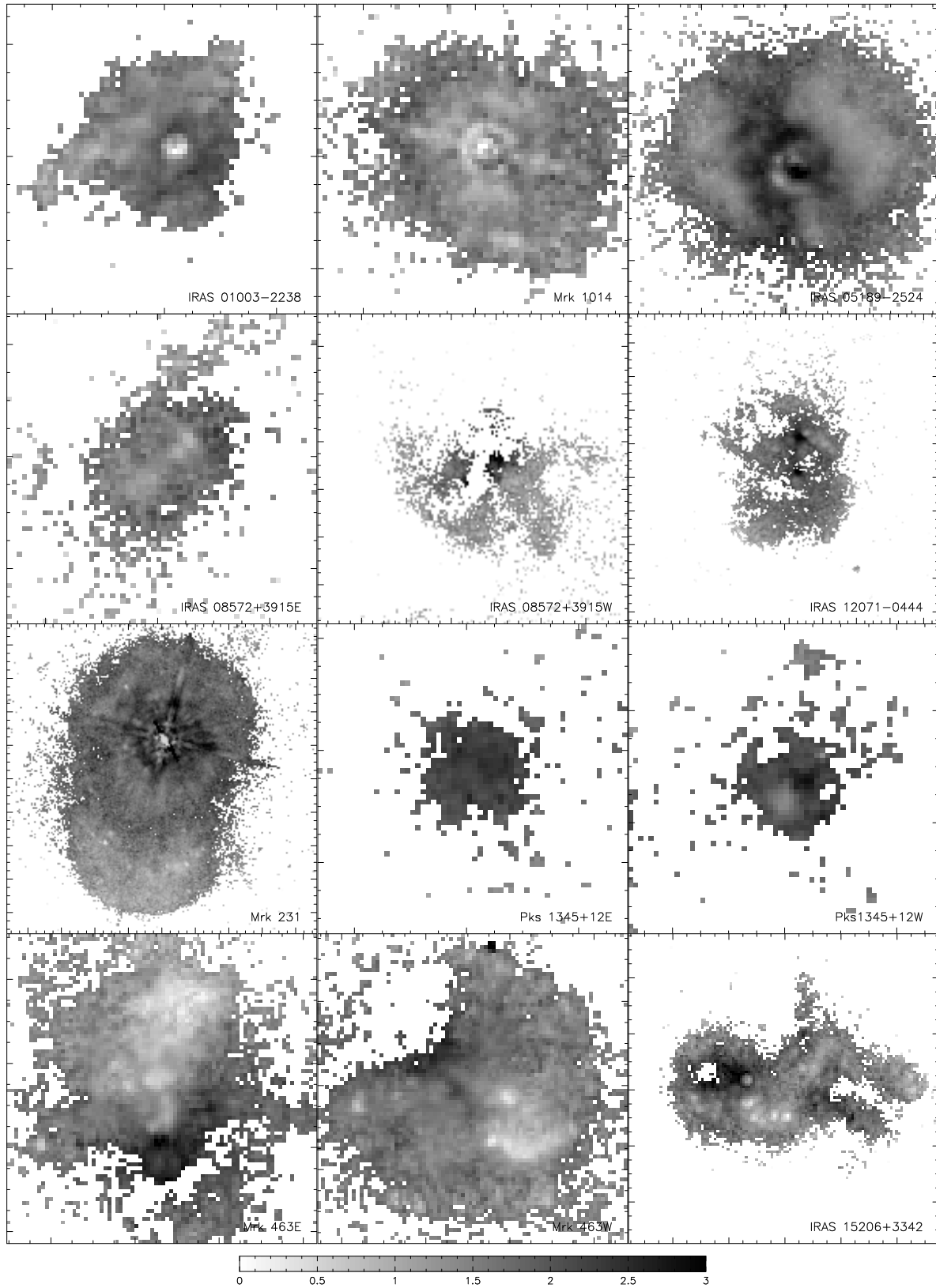


FIG. 6.— $B-I$ color maps of the nuclear regions of the warm ULIGs. The scale bar is the same as in Figs. 4 and 5. $B-I$ colors range from 0 to 3 (blue to red), except for PKS 1345 + 12, where they range from 0 to 4.

reliable uncertainty from measurement is about 0.15. Systematics due to calibration problems (see § 4) and aperture effects contribute another 0.1 mag. Since the systematics probably affect both filters nearly equally, the associated

uncertainty in color is only a function of measurement uncertainties and is around 0.2–0.3.

In almost every case, the knots appear to be resolved in comparison with both the observed PSF and the TIM

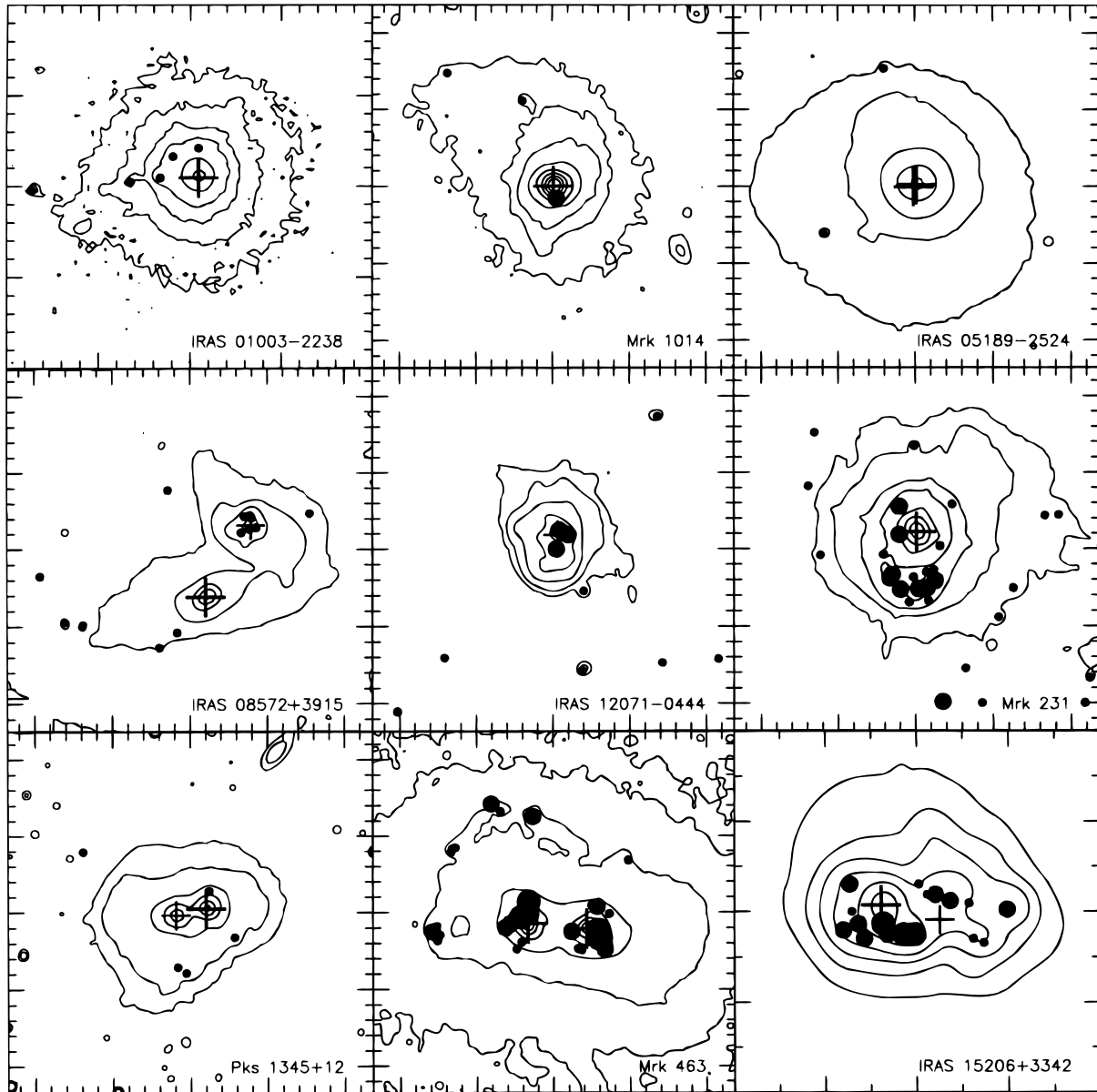


FIG. 7.—Locations of the identified blue knots superimposed on *I*-band contour maps of the warm ULIGs. The putative nuclei are indicated by crosses, and all other knots by filled circles. The contours have been smoothed for clarity. The orientation is the same as in Fig. 2.

models. Size measurements were performed by fitting radial Gaussians to the data using the IMEXAMINE task in IRAF. Each knot was fitted by hand in order to ensure that the centroiding and background estimation were reasonable, and that the actual fits were realistic. An effective radius, R_{eff} , was derived that is equal to the half-width at half-maximum (HWHM) of a Gaussian that, when convolved with the observed PSF, reproduces the measured width. These effective radii are given in Table 2.

The technique of using Gaussian fits to estimate effective radii has been employed by several workers (Whitmore & Schweizer 1995; Meurer et al. 1995), although others have argued that Hubble profiles with characteristic core and half-light radii may be more appropriate for knot measurements (Holtzman et al. 1996). Given that the data only

rarely have sufficient signal-to-noise ratio to detect the low, broad wings of the Hubble profile, and that radial Gaussians seem to provide very good fits to the detected knot profiles, use of Gaussians seems well motivated. Of course, the total luminosities of the knots will be affected by the actual form of the fitting function.

Simulations were performed in order to estimate the uncertainties of this technique. Gaussian distributions with sizes similar to the derived sizes were convolved with the observed PSF and rescaled to match the range of magnitudes of the observed knots. These were then added (with appropriate noise modeling) to the actual data in Mrk 231. In all cases, it was found that the derived width *overestimates* the real width, with this tendency increasing slightly as the signal-to-noise ratio decreases. It is likely that the

TABLE 2
WARM GALAXY KNOTS

Number	Δ R.A. (arcsec)	Δ Decl. (arcsec)	m_B (mag)	m_I (mag)	M_B^a (mag)	R_{eff}^b (pc)	Mass (M_\odot)
IRAS 01003–2238							
1	0.74	−0.05	24.25	23.43	−14.17	65	2E+07
2	0.41	0.00	23.50	23.16	−14.92	106	2E+06
3	0.28	0.23	23.27	22.78	−15.15	161	2E+06
4	0.00	0.32	23.82	23.77	−14.60	55	1E+06
5 ^c	0.00	0.00	19.27	18.32	−19.15	28	3E+08
Mrk 1014							
1	2.04	5.54	23.79	23.07	−15.37	70	3E+06
2	6.91	7.34	23.90	23.29	−15.26	80	3E+06
3	−0.22	−0.81	22.47	21.50	−16.69	150	4E+08
4 ^c	0	0	16.40	15.90	−22.76	<15	3E+09
IRAS 05189–2524							
1	5.93	−3.08	23.04	21.92	−13.14	12	2E+07
2	2.02	7.68	<24.68	23.13	<−11.15	64	...
3 ^d	−0.09	0.14	18.78	16.55	−17.40	25	2E+10
4 ^d	0.09	−0.09	19.01	17.37	−17.17	27	1E+09
IRAS 08572+3915							
1	13.55	−3.33	26.00	24.50	−10.86	74	4E+06
2	11.98	−6.27	24.14	23.38	−12.72	48	5E+06
3	10.83	−6.55	24.57	24.10	−12.29	49	2E+05
4	5.91	−7.93	24.58	24.35	−12.28	67	2E+05
5	4.76	−6.95	23.52	22.98	−13.34	65	4E+05
6	−3.80	0.76	24.92	24.23	−11.94	55	1E+05
7	5.36	2.28	24.08	24.08	−12.78	140	2E+05
8	0.62	−0.48	23.85	21.58	−13.01	26	3E+08
9	0.13	−0.25	24.59	22.28	−12.27	75	2E+08
10	−0.33	−0.16	23.43	22.75	−13.43	55	5E+05
11 ^c	0.00	0.00	22.90	20.59	−13.96	114	1E+09
12	−0.02	0.47	24.68	22.42	−12.18	102	1E+08
13	0.05	0.65	24.79	22.66	−12.07	71	9E+07
14	0.41	0.57	24.44	23.07	−12.42	40	1E+07
15 ^c	2.88	−4.66	20.54	19.26	−16.32
IRAS 12071–0444							
1	10.45	−11.44	<27.50	23.53	<−11.11	142	...
2	7.38	−7.96	27.41	24.04	−11.20	82	2E+09
3	−1.69	−3.64	23.55	22.78	−15.06	54	5E+07
4	−1.60	−8.79	<27.50	22.32	<−11.11	104	...
5	−6.81	−8.28	24.70	24.06	−13.91	17	8E+05
6	−10.44	−8.00	25.19	23.74	−13.42	120	4E+07
7	−6.49	7.73	25.71	23.24	−12.90	150	6E+08
8	0.09	−0.92	22.75	20.52	−15.86	202	4E+09
9 ^c	0.00	0.00	21.59	19.00	−17.02	244	4E+10
10	−0.09	0.32	21.61	20.19	−17.00	112	1E+09
11	−0.37	0.14	22.02	20.40	−16.59	126	8E+08
12	−0.69	0.00	22.66	21.59	−15.95	181	2E+08
13	−0.92	−0.23	23.55	22.33	−15.06	112	1E+08
Mrk 231							
1	1.10	1.68	22.23	21.12	−13.92	66	3E+07
2	−1.52	−0.90	23.27	20.86	−12.88	<20	5E+08
3	1.10	−0.16	22.38	20.86	−13.77	62	5E+07
4	2.12	−1.45	23.98	22.60	−12.17	42	1E+07
5	1.70	−2.97	21.31	20.50	−14.84	<20	4E+07
6	1.56	−2.74	22.97	22.28	−13.19	71	4E+05
7	1.01	−3.70	22.69	21.47	−13.47	38	3E+07
8	0.18	−2.92	24.60	23.10	−11.55	46	7E+06
9	0.46	−4.53	23.52	22.15	−12.63	51	2E+07
10	−0.14	−3.66	22.57	21.88	−13.58	46	6E+05
11	−0.46	−3.66	21.17	20.66	−14.98	136	2E+06
12	−0.69	−3.61	21.46	20.70	−14.69	31	3E+07
13	−0.78	−4.44	23.65	22.75	−12.50	25	6E+06
14	−1.20	−3.15	21.79	20.33	−14.36	40	9E+07
15	−0.64	−2.60	24.05	22.59	−12.10	<20	1E+07

TABLE 2—*Continued*

Number	Δ R.A. (arcsec)	Δ Decl. (arcsec)	m_B (mag)	m_I (mag)	M_B^a (mag)	R_{eff}^b (pc)	Mass (M_\odot)
16	−1.10	−2.46	24.15	23.54	−12.00	42	1E+05
17	6.58	6.51	24.80	24.12	−11.35	91	8E+04
18	0.14	5.64	23.28	21.64	−12.87	44	2E+07
19	6.21	−1.50	24.10	22.44	−12.05	46	2E+07
20	−1.70	−10.97	22.51	21.79	−13.64	44	7E+05
21	−4.23	−11.06	23.64	23.48	−12.51	46	2E+05
22	−3.17	−8.81	25.53	24.71	−10.62	65	8E+05
23	−10.81	−11.06	23.40	22.60	−12.75	43	5E+06
24	−11.13	−9.41	24.15	23.21	−12.00	<30	4E+06
25	−5.29	−5.50	25.49	23.71	−10.66	<20	7E+06
26	−6.21	−3.61	23.64	23.35	−12.51	43	2E+05
27	−8.23	1.08	23.34	22.69	−12.81	35	3E+05
28	−9.11	1.13	24.39	23.15	−11.76	183	5E+06
29	−2.30	1.82	23.26	21.06	−12.89	46	2E+08
30	6.99	3.01	26.08	24.59	−10.07	<20	2E+06
31°	0.00	0.00	14.54	12.99	−21.61	<20	7E+10
PKS 1345+12							
1	1.85	−3.76	23.64	22.86	−14.84	69	4E+07
2	1.29	−4.13	23.92	23.10	−14.56	97	3E+07
3	−1.83	−1.83	24.04	23.19	−14.44	162	3E+07
4	−0.18	1.16	24.23	22.52	−14.25	134	2E+08
5	7.92	3.74	<26.70	23.44	<−11.78	102	...
6°	1.93	−0.41	21.76	18.66	−16.72	165	1E+11
7°	0.00	0.00	20.64	17.91	−17.84	84	1E+11
Mrk 463							
1	9.79	0.11	23.23	22.58	−13.34	60	5E+05
2	10.10	−0.26	22.80	22.32	−13.77	48	6E+05
3	9.59	−0.45	24.30	23.24	−12.27	23	7E+06
4	9.74	−0.81	23.17	22.95	−13.40	39	4E+05
5	6.25	8.11	22.87	22.65	−13.70	82	5E+05
6	5.65	7.60	23.05	22.78	−13.52	52	4E+05
7	3.54	7.28	22.48	21.96	−14.09	48	9E+05
8	8.59	5.23	23.38	23.15	−13.19	42	3E+05
9	8.78	5.17	23.28	23.35	−13.29	49	3E+05
10	8.87	4.94	23.79	24.05	−12.78	48	2E+05
11	4.59	−1.37	24.24	24.13	−12.33	42	1E+05
12	4.27	−0.91	25.86	23.21	−10.71	25	1E+08
13	5.33	0.01	22.48	21.74	−14.09	36	2E+07
14	5.00	0.29	22.54	21.08	−14.03	121	6E+07
15°	3.85	0.29	18.83	16.95	−17.74	69	6E+09
16	4.31	0.70	20.87	20.78	−15.70	16	3E+06
17	3.81	1.72	20.28	20.52	−16.29	<20	4E+06
18	3.90	0.93	18.50	17.78	−18.07	83	4E+07
19	1.00	−0.22	21.69	20.68	−14.88	47	7E+07
20°	0.00	0.00	18.82	16.76	−17.75	58	1E+10
21	−0.70	−0.12	19.83	19.07	−16.74	50	2E+08
22	0.59	−1.32	23.47	23.21	−13.10	38	3E+05
23	0.36	−1.41	23.53	23.44	−13.04	24	2E+05
24	−0.29	1.49	22.81	22.34	−13.76	62	6E+05
25	−0.65	1.39	22.67	21.93	−13.90	65	1E+07
26	−1.44	0.93	24.00	23.00	−12.57	81	8E+06
27	−1.15	−1.37	22.95	23.08	−13.62	62	4E+05
28	−0.56	−0.68	21.50	21.41	−15.07	100	1E+06
29	−0.93	−0.77	20.88	20.82	−15.69	109	3E+06
30	−0.79	−0.72	20.86	20.82	−15.71	77	3E+06
IRAS 15206+3342							
1	0.69	0.46	21.77	21.96	−16.79	206	7E+06
2	0.64	−0.14	23.00	20.37	−15.56	73	3E+09
3	0.83	−0.55	22.30	20.94	−16.26	159	4E+08
4	0.51	−0.41	22.08	20.18	−16.48	76	2E+09
5	0.37	−0.74	22.60	21.23	−15.96	107	3E+08
6°	0.00	0.00	19.29	17.37	−19.27	57	3E+10
7	−0.05	−0.41	19.50	18.68	−19.06	104	2E+09
8	−0.14	−0.64	21.54	21.78	−17.02	84	8E+06
9	−0.51	−0.64	19.45	18.54	−19.11	88	3E+09
10	−0.74	−0.64	20.43	20.17	−18.13	67	3E+07
11°	−1.29	−0.32	22.87	20.10	−15.69	93	2E+10
12	−2.02	−0.74	22.66	20.83	−15.90	233	1E+09

TABLE 2—*Continued*

Number	Δ R.A. (arcsec)	Δ Decl. (arcsec)	m_B (mag)	m_I (mag)	M'_B ^a (mag)	R_{eff} ^b (pc)	Mass (M_\odot)
13	-2.25	-0.83	22.64	20.81	-15.92	221	1E+09
14	-0.83	0.46	23.33	21.79	-15.23	152	2E+08
15	-1.01	0.23	23.28	22.07	-15.28	90	1E+08
16	-1.20	0.23	22.37	21.75	-16.19	101	7E+06
17	-1.52	0.09	22.44	20.46	-16.12	108	2E+09
18	-1.93	0.05	23.73	21.91	-14.83	87	3E+08
19	-2.76	-0.09	21.74	20.55	-16.82	233	6E+08

NOTE.—Reference to the knots should be made in accordance with the *IAU* naming convention (galaxy name): SSVVM (number).

^a Absolute magnitude, uncorrected for redshift, as given by eq. (1).

^b Effective radius defined by half-width half-intensity.

^c Putative nucleus—identified on the basis of $B-I$ color, size, and absolute B magnitude (in all cases, the brightest object at B).

^d The two listed nuclei appear to actually be a single nucleus split by a dust lane.

actual knot sizes are somewhat smaller than those reported, although the simulations indicate that the uncertainty is probably not more than 40%. No significant correlation was found for observed width versus apparent magnitude; thus, it is likely that the correlation found in the simulations between derived width and S/N are not significant in the actual data. The tendency of this method to overestimate the true width has been noticed before (Schweizer et al. 1996).

Additionally, tests were performed to determine the effect of source extension on the derived magnitude. Assuming Gaussian radial distributions with the effective radii observed (typically 1.25–2 pixels), the additional aperture corrections needed compared with those derived from point-source models are very small (<0.05 mag) for the 4–7 pixel radius apertures used to determine the photometry.

5.3. Identification of Putative Nuclei

Within the general population of knots that were identified for each object, there were one or two knots which we believe plausibly represent putative nuclei. Not only are these the brightest knots at B , but they are also usually the most pointlike and connected to morphological features such as tidal tails (in the case of the double-nucleus systems), and, more importantly, they are spatially coincident with dominant K -band peaks in high-resolution K -band images that have recently been obtained with the University of Hawaii (UH) 2.2 m telescope (Surace et al. 1997). The properties of these putative nuclei can be found in Table 2, including the implausibly large masses that would be implied if these objects were interpreted as starbursts (see § 6.2).

6. DISCUSSION

6.1. Large-Scale Features

Of the nine warm ULIGs observed by us with *HST*, all but IRAS 01003–2238 are unmistakably advanced merger systems. This is perhaps expected since several recent studies have shown that greater than 95% of ULIGs are strongly interacting/merger systems (Sanders et al. 1988b; Melnick & Mirabel 1990; Kim 1995; Murphy et al. 1996; Clements et al. 1996). More interesting perhaps (and indeed what our *HST* observations were designed to show) is the mean separation of the nuclei of the parent disks. Although our statistics are obviously limited by the small sample size, we find that the warm ULIG double-nuclei fraction is con-

siderably lower than that of “cold” ULIGs. As will be shown later, following our discussion of the knots observed in each object, only four of the nine observed warm galaxies have obvious double nuclei (44%), as opposed to $\geq 60\%$ found by Murphy et al. (1996) for his ground-based images of cold ULIGs. Three of the four double-nucleus warm ULIGs were already known to be double from lower resolution ground-based observations. The enhanced resolution of *HST* has primarily revealed that what were previously thought to be possible doubles (e.g., based on oval-shaped inner contours in r -band images) in the case of IRAS 12071–0444 and IRAS 05189–2524 are more plausibly explained as complex clumps of many star-forming knots in the former and dust bifurcation in the latter. This lack of additional galaxy nuclei at very small separations may indicate either that the progenitor nuclei rapidly coalesce during the warm ULIG phase or that obscuration due to dust and/or confusion with star-forming regions can hide the second nucleus; however, we argue against this latter interpretation below. In general, the smaller fraction of double nuclei seems to support the idea that the warm ULIGs are more advanced mergers than the majority of ULIGs that have cooler far-infrared colors.

6.2. Knot Ages and Masses

Figure 8 shows the M'_B versus $(B-I)$ color-magnitude diagram for the individual knots in each of the nine warm ULIGs. (Those knots that were flagged in Table 2 as representing possible nuclei have been excluded from this plot and will be discussed separately in § 6.6). Typically, $0 < (B-I) < 2.5$. The limiting magnitude at B varies typically between $M'_B = -10$ (for Mrk 231) and $M'_B = -12.5$ (PKS 1345+12), although not all knots this faint are detected owing to confusion with the complex structure of the underlying galaxies. Detection is believed to be complete in all systems to about $M'_B < -12.5$.

Stellar synthesis models created by the GISEL package (Bruzual & Charlot 1993, hereafter BC93) are the basis for our estimates of the knot ages and masses. These models compute complete spectral energy distributions for different stellar ensembles with different star formation histories in time steps ranging from 0.5 Myr to 20 Gyr and produce absolute magnitudes in many standard filters. These models are based on solar metallicity; no attempt has been made to explore metallicity effects since they are most likely unimportant compared with other uncertainties. A Salpeter initial mass function (IMF) and a stellar mass distribution

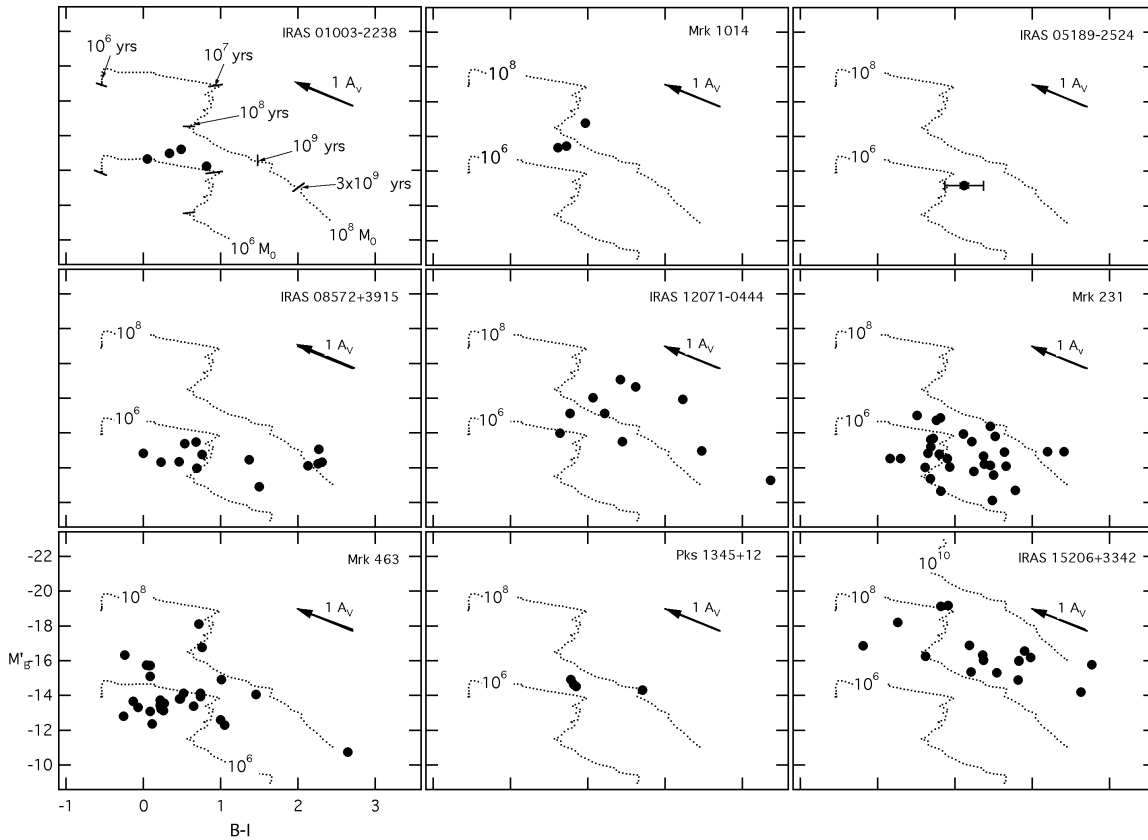


FIG. 8.—Color-magnitude diagrams, M'_B vs. $(B-I)$, for identified knots in the warm ULIGs. The dotted lines represent evolutionary tracks for instantaneous starbursts of 10^6 and $10^8 M_\odot$. The upper left-hand box (IRAS 01003–2238) marks the locations on the evolutionary tracks corresponding to the starburst age in years. The data in the upper right-hand box (IRAS 05189–2524) show error bars that are typical of the uncertainties in the $B-I$ colors of the knots in all of the warm ULIGs. These error bars are omitted on the remaining graphs for the sake of clarity. The dereddening vector ($A_V = 1$) is shown in the upper right-hand corner of each panel.

from 0.1 to $125 M_\odot$ are assumed, although the actual mass distribution has little effect after an age of a few Myr. This model is probably applicable to the majority of starburst regions (Leitherer 1996). The models were used to construct color-magnitude, M'_B versus $(B-I)$, evolutionary tracks as a function of time for an instantaneous starburst of different total masses (Fig. 8). They illustrate that the knot age is a nearly monotonically increasing function of $B-I$ color, although there is a degeneracy in $B-I$ colors from approximately 10^7 to 10^8 yr during which the color remains essentially fixed ($B-I = 0.7$). Perhaps not surprisingly, the mean knot color is very close to this value (Fig. 9). Our knot ages are determined entirely from the $B-I$ color since the constraints on the intrinsic knot luminosity are relatively weak. Knot masses are derived from the BC93 models by scaling a $1 M_\odot$ stellar ensemble to the observed absolute magnitude. The evolutionary tracks in Figure 8 are for knots of a fixed mass.

The effects of 1 visual magnitude of dereddening (Sapari & Kuusik 1978) are also shown in Figure 8. Kim (1995) examined optical spectra of five of the nine galaxies in our sample and concluded that the reddening varied typically from $A_V = 2$ mag (IRAS 15206+3342) to $A_V = 6$ mag (IRAS 08572+3915). Unfortunately, the slit size and extraction apertures of these spectra are so large that they are averaged over the entire central ($\approx 2''$) regions of the galaxies. The complex morphology in the *HST* images suggests that the actual extinction is likely to be patchy in many cases. Additionally, an examination of the *HST* data in the aper-

tures used for these spectra shows that the knots typically account for 10%–40% of the wide-band optical emission; they do not dominate it, and hence the reddening indicated by the spectra applies at least in part to either the underlying galaxy or the nucleus. It is unlikely that the reddening of the knots can be as large as that estimated by Kim (1995) since this would imply that the knots are intrinsically much

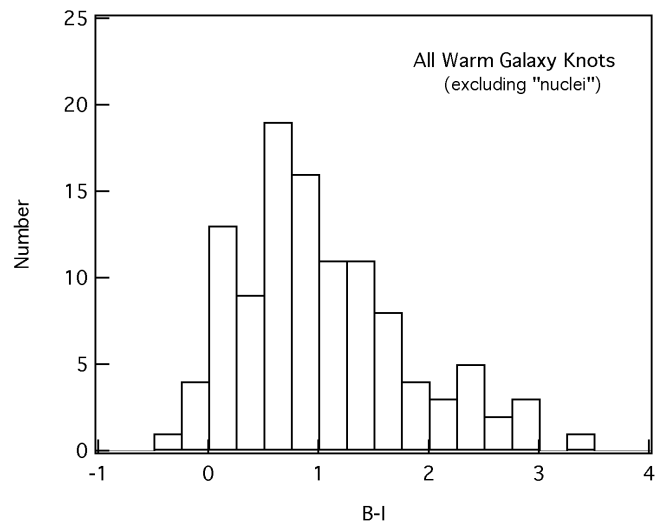


FIG. 9.—Distribution of $B-I$ colors for all of the knots (excluding putative nuclei) identified in all of the warm ULIGs.

bluer than even a zero-age starburst. Some authors (Whitmore & Schweizer 1995) have argued that the dust clearing time is likely to be very short, with a 100 pc region (roughly the size of our knots) being cleared in only 10^6 yr. Since we believe that these systems are at least 10–100 Myr or more in age, possibly very few of them still have substantial foreground dust screens and may not be very reddened. However, at least a handful (five) of the knots must be highly reddened, since they are redder than stellar aging can account for.

The dereddening vector lies nearly parallel to the evolutionary track. Hence, it is difficult, from *B*- and *I*-band observations alone, to distinguish between stellar aging and reddening, particularly in the absence of any knowledge of the intrinsic knot luminosities. The derived ages are thus upper limits. The ages are well constrained only for the very youngest knots, since they cannot be very reddened. However, the dereddening vector nearly parallels lines of constant mass, and hence dereddening has very little effect on the derived mass. The only difficulty arises when the knots have apparent colors of $(B-I) > 0.7$ yet have true (dereddened) colors of $(B-I) < 0.7$. In this case, our mass estimates based on the reddened colors will be too large by a factor of nearly 10. Otherwise, estimating the mass based on reddened colors will overestimate it by at most a factor of 2. All of the masses listed in Table 2 are therefore upper mass limits. Both the time degeneracy and the uncertainties due to reddening can be addressed with additional observations at shorter wavelengths (e.g., *U* band). From 10–100 Myr, $(B-I)$ (and all combinations of *B* and longer wavelengths) remains essentially fixed, while $(U-B)$ is evolving rapidly (Fig. 8). Furthermore, while in almost all two-color diagrams of *B* and longer wavelengths the evolutionary tracks parallel the reddening vector, the $(U-B)$ versus $(B-I)$ track is nearly perpendicular to the reddening vector. Alternately, high spatial resolution spectra would allow a direct measurement of each knot's reddening and stellar population.

Since we expect the properties of the knots to be connected to the galaxy merger system as a whole, we discuss below the mean properties of the knots on a *per galaxy basis*. Following Whitmore & Schweizer (1995), if it is assumed that the spread in knot colors is equally the result of the effects of reddening and intrinsic color due to age, then the mean reddening is $\sim 25\%$ of the spread in knot colors. The estimated mean reddening then varies from $A_V = 0.41$ mag in IRAS 15206+3342 to $A_V = 0.08$ mag in Mrk 1014. Applying no reddening correction, the knot colors imply ages varying from a mean of 7 Myr in Mrk 463 and IRAS 01003–2238 (corresponding to $\langle B-I \rangle = 0.4$) to 1.4 Gyr in IRAS 12071–0444 (corresponding to $\langle B-I \rangle = 1.63$). These represent upper limits to the mean knot ages in each galaxy. Applying the mean reddening correction shortens these ages to 6 and 370 Myr, respectively. The six remaining galaxies have upper limits to their mean knot ages of $\sim 6 \times 10^8$ yr (with no reddening correction). Note that if a reddening correction is applied to these six apparently older systems, then their ages may drop to as little as 0.6×10^8 yr owing to the degeneracy in $B-I$ colors from 10^7 to 10^8 yr. Due to the uncertainties involved, no further corrections will be made for reddening. The mean age for *all* knots in all warm ULIGs is 5.7×10^8 yr, while the median age is $(0.1\text{--}2.5) \times 10^8$ (the range being due to the color-age degeneracy). This latter figure is dominated

by the large numbers of blue knots in Mrk 463 and IRAS 01003–2238.

The five galaxies IRAS 01003–2238, IRAS 08572+3915, Mrk 231, Mrk 463, and IRAS 15206+3342 each contain at least a few knots whose ages cannot exceed 10 Myr. However, at the same time, the total span of colors is very large for some galaxies. The five galaxies IRAS 08572+3915, IRAS 12071–0444, Mrk 231, Mrk 463, and IRAS 15206+3342 all have many apparently old knots with ages 0.5–2 Gyr. This would seem to imply that either the knots are not all coeval or highly variable reddening is present. In the former case, some process initiated cluster formation (presumably the galaxy merger), but knot formation is then seen to continue for greater than 10^8 yr afterward. Meurer (1995) argues that NGC 4038/9 exhibits a cluster formation history similar to this.

Knots close to the galaxy centers seem to be much redder than those farther out. In particular, the two galaxies with the most well-developed, bright tidal tails (IRAS 08572+3915 and Mrk 463) both seem to have extremely blue knots ($\langle B-I \rangle \approx 0.34$ and 0.60 , respectively) in the tails that have age upper limits of only 6–10 Myr. The knots in the central regions of the galaxies are much redder, with implied ages of 30 Myr and 2 Gyr. This may reflect either differences in knot age, radially variable extinction ranging from $A_V = 0.5\text{--}2$ mag, or both.

There is a fairly wide range of derived knot masses spanning nearly 4 orders of magnitude, from a few times $10^5 M_\odot$ to a few times $10^9 M_\odot$. Individual globular clusters typically have masses of $10^5 M_\odot$ (van den Bergh 1995), while for the Whitmore & Schweizer (1995) knots and/or clusters we derive masses (based on the BC93 models) ranging from $10^{4.5}$ to $10^{6.5} M_\odot$. Even considering reddening effects, there are several galaxies that have knots that cannot be less than $10^8 M_\odot$ (IRAS 12071–0444 and IRAS 15206+3342), and other galaxies have knots that cannot be less than $10^7 M_\odot$. Figure 8 shows that the distribution of colors for any single object covers a wide range of color with a significantly smaller range in luminosity. This implies that the older knots are generally the most massive. If the spread in knot colors is primarily due to reddening, then the more massive knots must be preferentially more reddened than the less massive ones. This may be a selection effect: low-mass knots with extreme ages ($> 10^9$ yr) or reddening are too faint at *B* to still be detected. However, it is the case that, in the systems with many knots, *there are no young blue knots with estimated masses as large as the older, redder knots*. The above discussion of the correlation between color and radial distribution also extends to the knot masses: the most massive knots appear preferentially distributed closer to the galaxy nuclei.

6.3. Knot Sizes

There appears to be a considerable range in knot sizes. The resolution limit varied from around 10 to 30 pc, depending on the distance to the galaxy, and so a handful were unresolved, and it is not possible to rule out that these are stars. The remaining knots have an average R_{eff} of 65 pc, with the very largest being nearly 250 pc in radius. This is 2–3 times larger than the largest knots found in other systems, and many times larger than their mean knot radii: 18 pc in NGC 4038/9 (Whitmore & Schweizer 1995) and ~ 10 pc in nine starburst galaxies (Meurer et al. 1995). Schweizer et al. 1996 derives a median upper limit of 5 pc

for the clusters/knots in NGC 3921, and Holtzman et al. (1996) finds typically 2–10 pc. Our largest knots are nearly 50 times larger than these and the 1.5–5 pc half-light radii of globular clusters (van den Bergh, Morbey, & Pazder 1991).

6.4. Luminosity Function of Knots

Figure 10 presents the luminosity functions of the knots in Mrk 231 and Mrk 463, the two systems with the largest number of knots. These functions appear to be similar to the bright tail of the cluster/knot luminosity functions found in more nearby interacting galaxies such as NGC 4038/9 and NGC 7552. The data were binned into 0.5 mag bins, which are sufficiently large that photometric uncertainties should have little effect on the form of the distribution. Additionally, the putative “nuclei” have not been included, since they are believed to be of nonstellar origin (see § 6.5). A lower magnitude limit cutoff of $M'_B = -12.5$ was chosen to ensure completeness in both systems. There is no direct evidence of a turnover in the knot luminosity function. This is not surprising: if we assume an age of 600 Myr for most of the knots, and a peak in the current galactic globular cluster distribution near $M_B \approx -8$, then the peak would occur in our (younger cluster) data near $M_B = -12$, which is just fainter than our completeness limit. This makes the assumption that all the clusters are the same age; Meurer (1995) argues that the luminosity function of burst-model clusters with continuous cluster formation resembles more closely the power law observed by Whitmore & Schweizer (1995).

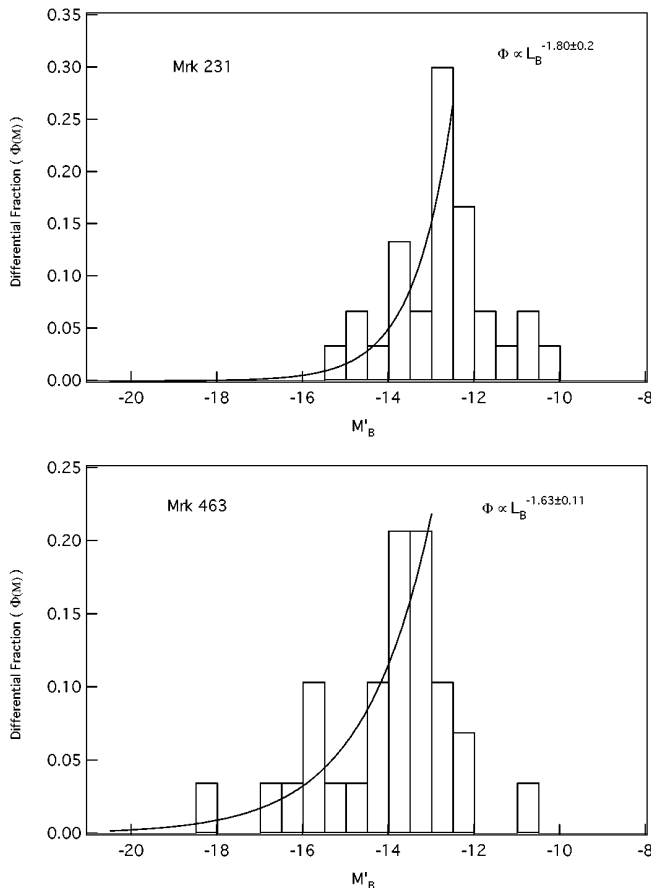


FIG. 10.—Luminosity functions for the knots (excluding putative nuclei) identified in Mrk 231 and Mrk 463.

A power-law fit of the form

$$d\Phi/dL'_B \propto L'_B{}^{-\alpha} \quad (2)$$

yields indices of $\alpha = -1.80 \pm 0.20$ and $\alpha = -1.63 \pm 0.11$ for Mrk 231 and Mrk 463, respectively. This index is surprisingly robust; moving the magnitude limit higher or removing the brightest objects seems to have little effect. This is similar to those found for compact knots/clusters in other systems: $\alpha = -1.78 \pm 0.05$ for NGC 4038/9 (Whitmore & Schweizer 1995), $\alpha = -2.1 \pm 0.3$ for NGC 3921 (Schweizer et al. 1996), and $\alpha = -1.64 \pm 0.07$ for NGC 1275 (Holtzman et al. 1996). However, combining the data for all the warm galaxies and choosing an appropriate limiting magnitude that ensures completeness in every system, we find $\alpha = -1.39 \pm 0.08$. This is appreciably more positive than that found in other systems and is due to an overabundance of bright knots. This may be partly contaminated by confusion owing to an inability to resolve the knots properly, as described below. Both Whitmore & Schweizer (1995) and Holtzman et al. (1996) report that their brightest clusters/knots have $M_V \approx -15.5$. We expect $(B-V) \leq 0.5$ based on BC93 for clusters of the ages determined by those authors; hence, the brightest observed knots in Mrk 231 are similar to those seen in more nearby systems. However, there are knots in Mrk 463 that are nearly 2.5 mag brighter than this, and in the warm ULIGs as a whole there are many knots (see IRAS 15206+3342 in Fig. 8) that are nearly 4 mag brighter than the brightest clusters/knots seen in other systems. Thus, there is a population of knots in the warm ULIGs that are nearly 100 times brighter at B than the brightest clusters/knots found in much closer interacting galaxies. The distribution of these knots is noticeably skewed such that there is an overabundance of bright knots, compared with the knots in nearby galaxies. Also, with typical estimated knot masses ranging from $10^5 M_\odot$ to as high as $10^9 M_\odot$, they vary from 10 to 500 times more massive than that estimated for the clusters/knots observed in other galaxies. If the brightest observed knots are single physical entities, then they lie on the extreme tail of the cluster/knot distribution seen in other galaxies, which is apparently normally unpopulated.

A more likely explanation is that the knots are associations of many of the clusters seen in nearer systems. Meurer (1995) notes that the typical intercluster separation in some starburst regions may be ≤ 18 pc, which is too small to resolve in our observations. We note that the seeing-limited resolution of NGC 4038/9 from the ground ($1'' = 90$ pc for $H_0 = 75 \text{ km s}^{-1}$) is similar to the diffraction-limited resolution of the warm ULIGs that can be achieved with *HST* (≈ 90 pc FWHM for IRAS 15206+3342). Ground-based images of the central regions of NGC 4038/9 at B show a looplike structure with bright embedded knots (Rubin, Ford, D'Odorico 1970). These knots (excluding the regions of the galaxy nuclei) have mean radii of ≈ 75 pc (derived from the 45 pc HWHM spatial resolution ground-based data using the methods described above), varying from nearly unresolved to as large as 150 pc. This is very similar to the range seen in the warm ULIGs. Whitmore & Schweizer (1995) have determined that each of these knots in NGC 4038/9 is actually composed of many smaller clusters. The mean number of clusters per knot is 13, and, correspondingly, the knot as a whole is on average 2.8 mag brighter than the individual clusters. Assuming that the clusters associate in knots in an essentially random way,

then shifting the NGC 4038/9 luminosity function by this amount results in the brightest knots being equivalent to $M_B \approx -18.5$. This is only a magnitude difference from the brightest of the knots seen in the warm ULIGs. The derived masses of the warm ULIGs are still somewhat too large. While the lowest mass knots in the ULIGs can be explained as aggregates of tens of typical clusters with spatial distributions of the kind seen in NGC 4038/9, the most massive ULIG knots, like those in IRAS 15206+3342, approach $10^9 M_\odot$. This would require some 10^4 globular clusters or 50 of the most massive clusters observed by Whitmore & Schweizer (1995). This could be explained either by a very large reddening correction that would reduce the knot mass estimate by a factor of 15, by knots with larger total numbers of clusters due to a higher density than those seen in galaxies like NGC 4038/9, or by a preferential spatial distribution wherein extremely massive clusters tend to form together. Similarly, the smaller luminosity function index (with corresponding overabundance of bright knots) may be due either to an intrinsic difference in underlying cluster luminosity distribution between the ULIGs and nearby interacting and starburst systems or to a preferential spatial grouping of clusters in knots (whereby the brightest knots have a disproportionate share of bright clusters, because they are either young or massive).

There is no observable relationship between knot size and mass; the intrinsic scatter in these two properties masks any expected $M \propto D^3$ relationship for constant density. There is a strong correlation between knot mass and color (and hence age). As was noted earlier, there are no young knots as massive as the older knots. By extension, there are no young (blue) knots as dense as the older (red) knots. The knot densities vary from 0.1 to $1000 M_\odot \text{pc}^{-3}$ (Fig. 11). This range is below that of globular clusters, which is perhaps not surprising if the knots are indeed composed of associations of clusters.

6.5. Contribution of Star-forming Knots to Galaxy Luminosity

It is possible to address the relationship of the observed knots to the high bolometric luminosity of these systems. The mean integrated B magnitude of the observed knots in individual warm ULIGs in our sample is $M_B = -16.4$,

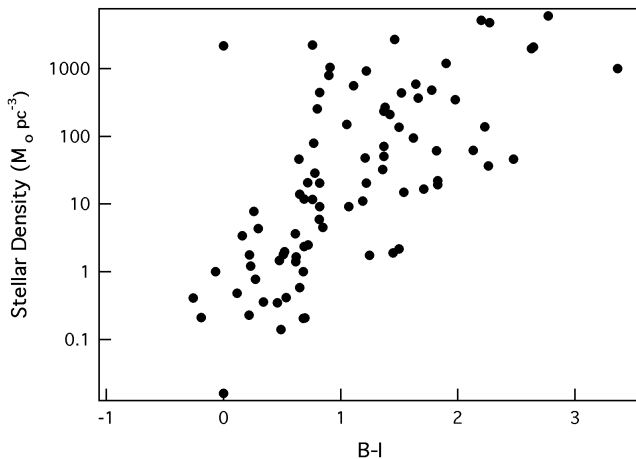


FIG. 11.—Mean stellar densities computed for all of the knots (excluding putative nuclei) identified in the warm ULIGs. There is a noticeable trend in that there are no blue knots with estimated masses or densities as large as the reddened knots.

ranging from -13.16 in IRAS 05189–2524 to a maximum of -20.4 for IRAS 15206+3342. A bolometric correction of 0.7 is derived from BC93 by assuming a starburst 600 Myr in age, consistent with the mean age previously derived on the basis of $B-I$ colors. Thus, generating the observed $\geq 10^{12} L_\odot$ in the far-infrared via the modeled starburst would require over 10^3 times more star formation than is presently observed in the B band in all of the starburst knots combined. Even in the most extreme example, IRAS 15206+3342, the total starburst bolometric luminosity derived from the observed B -band luminosity falls short by more than a factor of 40. Under the assumption of a younger, more luminous starburst (with an accompanying increase in the bolometric correction), which could be allowed by invoking the maximum allowable extinction of 2.4_ν , it would still require 100 times as much total star formation than currently exists in the observable knots in order to account for the observed far-infrared luminosity. The necessary luminosity would be possible to approach within a factor of 10 only in the case of IRAS 15206+3342. This result assumes that the knot SED is well modeled at nonoptical wavelengths by the spectral synthesis starburst model with uniform dust extinction. Local unresolved regions of high extinction internal to the knots will result in our underestimating the bolometric knot luminosity. Similar observations in the near-IR will be required to determine the near-IR excess, if any, of the knots.

Based on radio and far-infrared data, Condon et al. (1991) concluded that ULIGs contained ultraluminous starbursts in an environment so dense as to be optically thick even at $25 \mu\text{m}$. A deeply embedded ultraluminous starburst composed of star-forming knots with properties (luminosities and radii) similar to those optically observed would have to be at least 600–1200 pc in diameter. This is sufficiently large that it should be detectable in our images and color maps as a large region with a considerable color gradient ($B-I \geq 4$) or no detectable optical luminosity at all, although it might be possible to mask the presence of such a region with a peculiar overlying stellar distribution at lower optical depth. Such a large color gradient is detected only in IRAS 08572+3915 and IRAS 15206+3342, but only in the latter does this region approach 1 kpc in size. That such a large region is not generally observed in our data suggests that any ultraluminous starburst must be far more compact than the observed starburst knots, and that the spatially extended optical starburst is unlikely to share many properties with it. This is not surprising, considering that Condon et al. (1991) finds that ULIGs with $L_{\text{fir}} > 10^{12} L_\odot$ have radio emission typically dominated by compact radio sources. The three targets in the warm sample that he specifically examined have characteristic radio core sizes ranging from 0.1 to 80 pc in radius; additionally, Mrk 1014 (Kellerman et al. 1994), PKS 1345+12 (Shaw, Tzioumis, & Pedlar 1992), and Mrk 463 (Mazzarella et al. 1991) are also known to have compact cores. Based on the radio/far-infrared correlation, it is argued that the starburst energy source is of a similar size. The minimum blackbody radii Condon et al. derived from the far-infrared luminosities, which presumably are representative of the size of the enshrouding dust, are $0''.15 = 150 \text{ pc}$ for IRAS 05189–2524, $0''.09 = 85 \text{ pc}$ for IRAS 08572+3915, and $0''.25 = 200 \text{ pc}$ for Mrk 231. A single observed optical knot is similar to or larger than the expected size of the starburst region, and it is nearly one-

tenth as large as the volume of the dust shroud. Although such an obscured region containing very extreme star formation is not clearly seen, its detection is complicated by the uncertainties in coordinate precession and in the relationship between the radio and optical coordinate systems (Taff et al. 1990). These uncertainties prevent the registration of the radio and optical images with a precision greater than the typical spatial scale of the structure seen with *HST* ($\leq 0''.3$), making it impossible to pinpoint the location of the putative ultraluminous starburst. Thus, it is not possible to rule out conclusively an extremely compact, deeply embedded ultraluminous starburst, but it is possible to constrain its position and size, and to show that it cannot have properties similar to the starburst that we have actually been able to detect.

6.6. Putative Nuclei

Most of the warm ULIGs possess optical sources that are more luminous than the general knot population. The presence in these systems of optical emission lines typical of Seyfert galaxies suggests the presence of optically detectable active nuclei, thus providing an initial physical motivation for singling out these regions as putative “nuclei.” The magnitudes, sizes, and positions of the putative nuclei were measured, and they appear in Table 2 indicated by a footnote. In the cases of IRAS 08572+3915 (west), IRAS 12071–0444, Mrk 463 (east and west), and IRAS 15206+3342, it is not clear what constitutes an optical “nucleus”; in these cases, the brightest object seen at *B* was used. IRAS 05189–2524 lists both blue knots seen in the center of the galaxy. In most cases, the putative nuclei are also more pointlike than the general knot population. In the apparent double-nucleus systems (IRAS 08572+3915, PKS 1345+12, Mrk 463, and IRAS 15206+3342), one of these nuclei is more extended than the other and is likely to be the stellar core of one of the merging galaxies, as opposed to an active nucleus.

Figure 12 shows a color-magnitude diagram for the nuclei with the same scaling as Figure 8. QSOs have

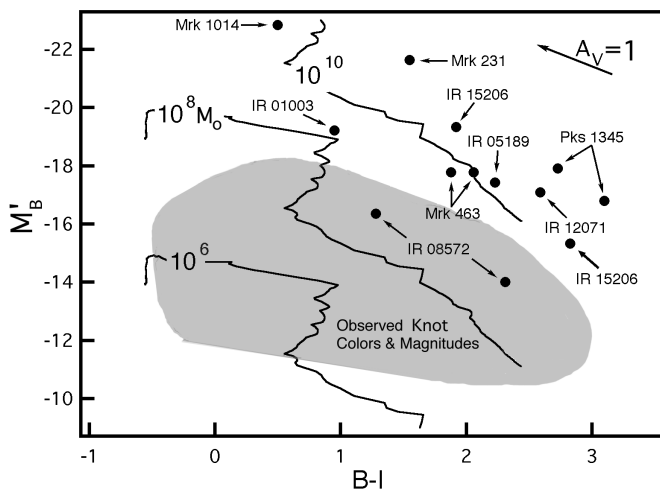


FIG. 12.—Color-magnitude diagram, M_B' vs. $(B-I)$, for the putative nuclei identified in each of the warm ULIGs. For comparison with the remaining knots, the shaded region indicates the locus of points for the data used in Fig. 8. Extinction ($A_V = 1$) is indicated by the dereddening vector in the upper right-hand corner. Mrk 1014, a PG QSO, is typical of the colors found in optically selected QSOs. The nuclei for the remaining warm ULIGs in our sample fall roughly along what can be described as a QSO reddening line.

$\langle B-I \rangle = 1.2 \pm 0.3$ (Elvis et al. 1994) with a *B* magnitude classically defined as $M_B < -23$ (Schmidt & Green 1983). Mrk 1014, a classical optically selected QSO, falls roughly within this region and represents a “zero point” in the color-magnitude diagram for “infrared-loud” classical QSOs. Three of the eight galaxies (Mrk 231, IRAS 15206+3342, and PKS 1345+12) have nuclei that fall very nearly on a reddening line extending through the data point for Mrk 1014 (see Fig. 12), and that therefore have QSO-like luminosities ($L_{\text{bol}} > 10^{12} L_{\odot}$), assuming they also have similar SEDs. In the case of Mrk 231, this is not surprising, since, optically, it appears much like a classical QSO. Morphologically, these nuclei share a common trait: all of them are very nearly radially symmetric in profile, which suggests that the underlying QSO nucleus is seen through a uniform foreground dust screen. We note that the reddening derived by Kim (1995) for PKS 1345+12, which has almost no knots and therefore has an optical spectrum probably dominated by the nucleus, is $A_V = 3.8$. This is similar to the reddening derived by assuming a reddened QSO nucleus ($A_V = 3.5$). The nuclei of Mrk 463, IRAS 12071–0444, IRAS 05189–2524, and IRAS 08572+3915 all show clear signs of complex extinction and scattering. Since the nuclei were defined to be a single component at *B*, any true nucleus affected by variable extinction and scattering would be both fainter and bluer than it would if the extinction were uniform. This would move it to the lower left-hand corner of the color-magnitude diagram, in the manner seen. IRAS 01003–2238 cannot be easily explained in this scenario, since it has a nearly stellar radial profile, yet falls considerably short of QSO-like luminosity. If the knots identified as nuclei are not actually QSO-like active nuclei but are instead compact luminous starbursts, then their derived bolometric luminosity (excluding Mrk 1014 and Mrk 231) is only about $10^{10} L_{\odot}$. Under the most extreme assumption that they are very young starbursts (1 Myr), their dereddened luminosities are as high as $2 \times 10^{11} L_{\odot}$.

We also note that the masses derived for the nuclei, under the assumption that they are a starburst of the sort modeled for the blue knots, are typically greater than $10^{10} M_{\odot}$. This seems unreasonably large in light of the measured radii. In the case of Mrk 231 and Mrk 1014, this would result in average stellar densities of nearly 10^7 and $2 \times 10^5 M_{\odot} \text{ pc}^{-3}$, respectively. Similarly, IRAS 01003–2238, IRAS 05189–2524, and PKS 1345+12 all have derived stellar densities greater than $10^5 M_{\odot} \text{ pc}^{-3}$. Elliptical galaxy cores typically have masses as high as $10^{10} M_{\odot}$, but they also have much smaller densities of $\approx 10^2$ – $10^3 M_{\odot} \text{ pc}^{-3}$. Similarly, although nuclear star clusters in galaxy cores may have very high densities ($> 10^5 M_{\odot} \text{ pc}^{-3}$), they have smaller masses ranging from 10^6 to $10^8 M_{\odot}$ (Lauer 1989). The remainder of the warm ULIG nuclei would require stellar densities of $10^3 M_{\odot} \text{ pc}^{-3}$ and higher, which makes them denser than all but seven of the knots and at the high end of elliptical core densities. The only exception is the eastern nucleus of IRAS 08572+3915, whose luminosity and color are consistent with a typical galaxy core, which it strongly resembles (see the Appendix).

Until high spatial resolution spectra are obtained, it will not be possible to determine whether or not the observed optical Seyfert activity is related to the putative nuclei that have been identified here. An interesting prediction of Condon et al. (1991) is that the observed broad optical emission line regions are a result of starburst/superwind

activity and must be extended on size scales larger than the minimum far-infrared size ($\geq 0''.25$). This minimum size is larger than the observed sizes of the putative nuclei. If the optical emission features are spatially coincident with and have size scales similar to the putative nuclei, then this may be strongly suggestive of a true active nucleus, rather than a spatially extended wind.

6.7. Relationship to Optical QSOs

One of the original motivations for studying our complete sample of warm ULIGs was that they might plausibly represent an important “transition stage” in the evolution of cooler ULIGs into optically selected QSOs. While the connection between the cool and warm ULIG samples seems fairly secure owing to the fact that ground-based observations have clearly shown that both samples are dominated by molecular gas-rich mergers (cf. review by Sanders & Mirabel 1996), the connection between warm ULIGs and optically selected QSOs is much less secure. This has been due in large part to a lack of sensitive high-resolution observations of QSO hosts coupled with the fact that the merger features, which are already hard to detect in many of the warm ULIGs, may fade to undetectability by the time these objects emerge as optical QSOs.

HST images of the three objects in our complete sample of 12 warm ULIGs that were not observed in our cycle 5 GO program either have been published recently or can be found in the *HST* archive. These three have the smallest far-infrared/submillimeter excess of the 12 warm ULIGs, and all of them exhibit Seyfert 1 optical spectra. Of the three, I Zw 1 and 3C 273 are well-known optical QSOs, while IRAS 07598+6508 has a Seyfert 1 optical spectrum that has led it to be featured as an “infrared quasar” in several recent publications (e.g., Low et al. 1988). These three (along with Mrk 1014) are both “warm” ULIGs and optical QSOs, and they represent the clearest transition between the two. Although the exposure times for these three sources were generally shorter than those used in our cycle 5 observations, and different filters were used, it is still instructive to compare their properties with what has been described above for the other nine sources observed by us in our complete sample. In particular, IRAS 07598+6508 and I Zw 1 have several properties in common with our data, including luminous knots and armlike circumnuclear features, as well as luminous hosts, although 3C 273 has yet to reveal knots or other large-scale features, other than its jet and the presence of a luminous host.

Additional recently published *HST* images of other nearby optically selected QSOs (Bahcall et al. 1997) further strengthen the evolutionary connection between warm ULIGs and QSOs. In particular, “arcs,” “loops,” and “chains of emission nebulae” seen in some of the 20 QSO hosts imaged by Bahcall et al. (e.g., PKS 2349–014, PG 0316-346), the double nuclei and/or partially merged disks seen in a few objects (e.g., PG 1012+008), and the “knots” of emission close to the QSO nucleus seen in the majority of the sample of QSOs all suggest a continuity of morphological properties with our sample of warm ULIGs. Further evidence for a connection comes from the fact that the mean absolute magnitude at both *r* band and *K* band of the host galaxies in the two samples appears to be nearly equal (e.g., Sanders & Mirabel 1996). Additional *HST* data, in particular spectroscopy of the emission knots discovered in both samples, may provide sufficient evidence to show whether

or not the features observed in QSO hosts are indeed aged versions of those observed in the warm ULIGs.

7. CONCLUSIONS

From our new *HST* WFPC2 images of a nearly complete sample of warm ULIGs, we draw the following conclusions:

1. Eight of the nine objects that were imaged show evidence that they are advanced merger systems. Three have clearly identified double nuclei, while an additional five objects show circumnuclear features that connect to larger scale tidal tails, fans, and/or bridges that were previously identified in lower resolution ground-based images.

2. A population of compact, blue star-forming knots has been discovered in all of the warm ULIGs. These knots appear similar in radius and luminosity to the most luminous knots found in ground-based images of nearby merger luminous infrared galaxies such as NGC 4038/9 and Mrk 171. *HST* imaging shows that the luminous knots in these nearby systems break up into groups of several massive star clusters that are assumed to be proto-globular clusters. However, the warm ULIGs are too distant to be similarly resolved with *HST*.

3. The masses of the star-forming knots in the warm ULIGs are estimated to be in the range 10^5 – $10^9 M_\odot$. There is some evidence that the warm ULIGs have an overabundance of luminous (massive) knots compared with other nearby, less luminous merger systems. Their (extinction-uncorrected) colors yield a median upper age for the starburst knots in a given system of $\sim 3 \times 10^8$ yr. Regardless of reddening effects, several of the systems have knots that must be very young [$\approx (0.5$ – $1) \times 10^7$ yr]. These young, blue knots are often found at larger radii, whereas those found closer to the centers are often redder. This color difference may be due to either radially variable extinction or knot age.

4. The combined total luminosity of the knots identified in our *HST* images of each system is generally too small by factors of 100 or more to account for the total observed far-infrared luminosity. If the far-infrared luminosity were the result of starburst activity in a large population of hidden knots similar to the ones detected optically, they would need to occupy a volume so large that it should be detectable in our observations. Any ultraluminous starburst is therefore likely to be very different from the starburst that is detected optically. Most likely, it will be much more luminous, massive, and dense than the identified starbursts knots.

5. In each system, we have identified one or more candidate knots as putative nuclei. These nuclei appear to have properties substantially different from the starburst knots. Their luminosities and colors would only be consistent with starburst models with an extremely biased high-mass IMF, and even then their relatively small apparent physical sizes would imply extraordinarily high stellar densities. Nearly all of these knots have colors and luminosities that can be more easily explained as reddened AGNs. High spatial resolution spectroscopy with *HST* could help prove that these extremely luminous knots are indeed the active nuclei that dominate the ground-based optical spectra of these objects.

We would like to thank Dong-Chan Kim for lending us his ground-based images and spectra of the ULIGs, John Hibbard for his images of NGC 4038/9, and Stéphane

Charlot for use of his GISSEL spectral synthesis libraries. We also thank an anonymous referee for his or her comments that have helped us clarify our results. D. B. S. and J. A. S. were supported in part by NASA through grant number GO-05982, and NASA grant NAGW-3938. W. D. V. acknowledges support in the form of a Fellowship from the Beatrice Watson Parrent Foundation. S. V. gratefully acknowledges the financial support of NASA through grant number HF-1039.01-92A awarded by the Space Telescope Science Institute, which is operated by the AURA, Inc., for NASA under contract NAS 5-26555. This work has made use of the NASA/IPAC Extragalactic Database

(NED), which is operated by the Jet Propulsion Laboratory, California Institute of Technology, under contract with the National Aeronautics and Space Administration, and the Digitized Sky Survey (DSS), which was produced at the Space Telescope Science Institute under US Government grant NAGW-2166. The DSS was produced using photographic data obtained with the Oschin Schmidt Telescope on Palomar Mountain, operated by the California Institute of Technology, and the UK Schmidt Telescope, which was operated by the Royal Observatory Edinburgh and the Anglo-Australian Observatory.

APPENDIX

NOTES ON INDIVIDUAL OBJECTS

The following notes on individual objects are added here to further help understand the relationship of the new *HST* imaging data (e.g., Figs. 2, 3, and 4) to previous ground-based observations (e.g., Fig. 1), as well as provide additional information on features that can be identified in the digital images (available from the *HST* archive) but that may not be so obvious in the hard copy figures.

I Zw 1.—Optical images of *I Zw 1* that exist in the *HST* archive reveal armlike features in the nuclear regions of the surrounding host galaxy, but these images are generally not deep enough to compare easily with our data. We have obtained ground-based optical images using tip-tilt optics on the UH 2.2 m telescope (Surace et al. 1997) that show more clearly the presence of features such as those seen in our *HST* images of Mrk 231, but there is no other obvious large-scale evidence of tidal structure.

IRAS 01003–2238.—This galaxy is the most pointlike of any in the sample. The only easily identifiable circumnuclear feature is a chain of knots extending from SE to NW, less than $1''$ away from the apparent nucleus. These knots are embedded in a plateau of extended emission. *IRAS 01003–2238* is known to be an unusually powerful Wolf-Rayet galaxy (Armus, Heckman, & Miley 1988), which is consistent with the young ages that can be assigned to the extremely blue knots.

Mrk 1014 = PG 0157+001.—An optically identified QSO (Schmidt & Green 1983) with a strong infrared excess (e.g., Sanders, Scoville, & Soifer 1988a). The underlying host galaxy is dominated by what appears to be a prominent tidal arm that curves toward the east, and a weaker counterarm that extends from the southwest and then curves to the north. There are two extremely blue knots, as well as several linear structures within 1 kpc of the QSO nucleus. Several other knots are found in the outer regions of the host.

IRAS 05189–2524.—Optically classified as a Seyfert 2 galaxy (Veilleux et al. 1995). The *HST* images clearly show that the plateau of emission seen in ground-based images to the southeast of the nucleus is resolved into at least two loops ≈ 15 kpc in total length at right angles to each other; additionally, there appear to be looplike or shell-like structures at slightly fainter levels. Although not visible here, careful analysis of the PC and adjoining WF frames reveals the two “hornlike” tidal features to the north seen in the ground-based image (see Fig. 1), and this analysis indicates that they are actually the high surface brightness base of a complete loop. There is no obvious connecting feature in the *HST* images that would connect the inner disk structure to the counter tidal tail previously identified by Sanders et al. (1988b) that extends to the south from the western edge of the disk.

IRAS 07598+6508.—The *HST B*-band image of *IRAS 07598+6508* obtained by Boyce et al. (1996) clearly shows several “chains” of “knots” surrounding the prominent optical nucleus, similar to the features seen by us in Mrk 231. In addition, large-scale tidal features have been detected in deep ground-based optical images obtained at the UH 2.2 m telescope (A. Stockton 1997, private communication), leading us to describe this object as a clear case of an advanced merger.

IRAS 08572+3915.—The new *HST* images clearly show the interaction of two spiral galaxies that have not yet merged. The eastern nucleus is morphologically similar to a spiral bulge from which a tidal tail 30 kpc in length emerges to the east and then wraps entirely around the system to the northwest. Another tidal tail at least 15 kpc in length emerges from the western nucleus and extends directly north. A bridge of material is seen connecting the two nuclei. Unlike the nondescript eastern nucleus for which we find no published reference as to spectral type, the LINER western nucleus (Veilleux et al. 1995) is morphologically complex, with several bright blue knots as well as highly reddened regions. This disparity in optical appearance is not surprising and probably reflects very real differences in the environments of these two nuclei. This is supported by studies at $3.4\ \mu\text{m}$ (Zhou, Wynn-Williams, & Sanders 1993), $10\ \mu\text{m}$ (Sanders et al. 1988c), and 1.66 GHz (Sopp & Alexander 1991) indicating that most of the bolometric luminosity of this object originates in the northwest nucleus.

IRAS 12071–0444.—Sanders et al. (1988c) classify this galaxy on the basis of optical spectra as a Seyfert 2. In addition, Veilleux, Sanders, & Kim (1997) find strong evidence for a “buried QSO” on the basis of detection of [Si VI] emission in the near-infrared. The *HST* images show two tidal tails extending to the north and south. The southern tail loops back around to the northeast (although it is difficult to see in Fig. 2) and appears to return almost to the nucleus, a total distance of 60 kpc; our *HST* images are not deep enough to tell if it reconnects. The inner 5 kpc region has a high surface brightness and is chaotic in appearance. A central, highly reddened compact source dominates this region. A string of blue knots 2.5 kpc in length runs to the west of the central source.

3C 273.—*HST* images of the radio-loud QSO 3C 273 (Bahcall et al. 1997), as well as previous ground-based images by us and others, clearly show an optical “jetlike” feature extending to the southwest from the optical nucleus and reveal the presence of a fairly luminous host galaxy. However, there is no obvious evidence of a previous interaction/merger, and the extreme brightness of the nucleus as well as the relatively short *HST* exposure times make the identification of any circumnuclear knots that might be present extremely difficult.

Mrk 231 = UGC 8058.—This optically classified Seyfert 1 galaxy is the most luminous object in the local ($z < 0.1$) universe (Sanders et al. 1988b). The *HST* data clearly show a diffuse linear structure to the NW of the Seyfert nucleus. The central kiloparsec shows the compact ($R_{\text{eff}} < 20$ pc) Seyfert nucleus surrounded by a system of concentric spiral features similar to spiral arms. However, these features appear to be off-center and cross each other on the eastern side where they then connect to the outer tidal features, allowing one to trace the outer tidal arms all the way into the central kiloparsec. Armus et al. (1994) claimed detection of a second nucleus in the near-infrared lying $3''$ to the south. However, the new *HST* images show this feature to be a dense arc of star-forming knots with a total estimated luminosity compatible with the extreme luminosities cited in that paper. Most of the compact blue knots detected by *HST* occur either in this arc or in the “plateau” to the west.

PKS 1345+12 = 4C 12.50.—The western nucleus is optically classified as a Seyfert 2 galaxy (Gilmore & Shaw 1986). More recently, Veilleux et al. (1997) have reported the detection of very broad Pa α emission in the near-infrared, indicating the likely presence of a “buried QSO.” The system also contains a compact gigahertz-peaked, compact-steep-spectrum radio source with a characteristic double-lobed shape in VLBI images that Shaw et al. (1992) associate with the eastern nucleus (although Stanghellini et al. 1993 associate it with the western nucleus!). Shaw et al. (1992) also interpret this object as a merger between a spiral Seyfert galaxy and a powerful radio elliptical galaxy. The extremely red color of this source ($B-I \approx 3.5$) has been attributed to dust obscuration (Smith & Heckman 1989). Our images show two radially symmetric nuclei with only a few additional compact blue knots. The western nucleus shows a slightly asymmetric color profile, whereas the eastern nucleus shows almost no color gradient at all.

Mrk 463 = UGC 8850.—The eastern nucleus is optically classified as a Seyfert 1 galaxy (Miller & Goodrich 1990). A radio luminosity density, aligned radio structures, and optical/near-infrared colors that have been interpreted by Mazzarella et al. (1991) as representative of a dusty QSO are associated with this nucleus. An optical “jet” seen by Uomoto et al. (1993) resembles in our data an X-shaped structure dominated by a central peak. Tremonti et al. (1996) report that the bright object to its north is highly polarized and reflects a hidden Seyfert 1 nucleus lying in this X-structure. This is confirmed by high-resolution near-infrared observations (Surace et al. 1997) that indicate that the near-infrared luminosity is centered on the X. The entire eastern nucleus lies on a plateau of extended emission in which there are several bright knots. The western nucleus is optically classified as a Seyfert 2. There seem to be two principal components to the western nucleus: a dominant source that is distinctly elongated in the E-W direction and a more compact, very blue source $1''$ to its west. Two arcs of star-forming knots to the north and south of the two dominant components of the western nucleus are also in this region. Both of these arcs form a sharp edge to a fan of emission centered on the dominant nuclear components.

IRAS 15206+3342.—Sanders et al. (1988c) classify this galaxy as a Seyfert 2 on the basis of optical spectra. The inner few kiloparsecs are characterized by many chains of knots, some of which are extremely luminous. Several of the knots have luminosities and colors compatible with being extremely massive starbursts, but there are two that make good candidates for being nuclei. Additional spectroscopic observations will be needed to identify unambiguously the source of Seyfert galaxy activity.

REFERENCES

- Armus, L., Heckman, T. M., & Miley, G. K. 1988, *ApJ*, 326, 45
 Armus, L., Surace, J. A., Soifer, B. T., Matthews, K., Graham, J. R., & Larkin, J. E. 1994, *AJ*, 108, 76
 Bahcall, J. N., Kirhakos, S., Saxe, D. H., & Schneider, D. P. 1997, *ApJ*, 479, 642
 Bahcall, J. N., Kirhakos, S., & Schneider, D. P. 1995, *ApJ*, 450, 486
 Boyce, P. J., et al. 1996, *ApJ*, 473, 760
 Bruzual A., G., & Charlot, S. 1993, *ApJ*, 405, 538 (BC93)
 Clements, D. L., Sutherland, W. J., McMahon, R. G., & Saunders, W. 1996, *MNRAS*, 279, 477
 Condon, J. J., Huang, Z.-P., Yin, Q. F., & Thuan, T. X. 1991, *ApJ*, 378, 65
 Elvis, M., et al. 1994, *ApJS*, 95, 1
 Gilmore, G. F., & Shaw, M. A. 1986, *Nature*, 321, 750
 Holtzman, J., et al. 1995a, *PASP*, 107, 156
 ———. 1995b, *PASP*, 107, 1065
 ———. 1996, *AJ*, 112, 416
 Kellerman, K., Sramek, R., Schmidt, M., Green, R., & Shaffer, D. 1994, *AJ*, 108, 1163
 Kim, D.-C. 1995, Ph.D. thesis, Univ. Hawaii
 Kim, D.-C., & Sanders, D. B. 1997, *ApJ*, submitted
 Krist, J. 1994, *The Tiny Tim User's Manual* (Baltimore: STScI)
 Lauer, T. 1989, in *Dynamics of Dense Stellar Systems*, ed. D. Merritt (Cambridge: Cambridge Univ. Press), 3
 Leitherer, C. 1996, in *ASP Conf. Ser. 98, From Stars to Galaxies*, ed. C. Leitherer, U. Fritze-von-Alvensleben, & J. Huchra (San Francisco: ASP), 373
 Low, F. J., Huchra, J. P., Kleinmann, S. G., & Cutri, R. M. 1988, *ApJ*, 287, 95
 Lu, N. Y., Hoffman, G. L., Groff, T., Roos, T., & Lamphier, C. 1993, *ApJS*, 88, 383
 Mazzarella, J., Gaume, R., Soifer, B. T., Graham, J. R., Neugebauer, G., & Matthews, K. 1991, *AJ*, 102, 1241
 Melnick, J., & Mirabel, I. F. 1990, *A&A*, 231, L9
 Meurer, G. 1995, *Nature*, 375, 742
 Meurer, G., Heckman, T., Leitherer, C., Kinney, A., Robert, C., & Garnett, D. 1995, *ApJ*, 110, 2665
 Miller, J. S., & Goodrich, R. W. 1990, *ApJ*, 355, 456
 Murphy, T., Armus, L., Matthews, K., Soifer, B. T., Mazzarella, J. M., Shupe, D. L., Strauss, M. A., & Neugebauer, G. 1996, *AJ*, 111, 1025
 Peebles, J. 1993, *Principles of Physical Cosmology* (Princeton: Princeton Univ. Press)
 Perault, M. 1987, Ph.D. thesis, Univ. Paris
 Rubin, V., Ford, W., & D'Odorico, S. 1970, *ApJ*, 160, 801
 Sanders, D. B., & Mirabel, I. F. 1996, *ARA&A*, 34, 749
 Sanders, D. B., Scoville, N. Z., & Soifer, B. T. 1988a, *ApJ*, 335, 1
 Sanders, D. B., Soifer, B. T., Elias, J. H., Madore, B. F., Matthews, K., Neugebauer, G., & Scoville, N. Z. 1988b, *ApJ*, 325, 74
 Sanders, D. B., Soifer, B. T., Elias, J. H., Neugebauer, G., & Matthews, K. 1988c, *ApJ*, 328, 35
 Sapar, A., & Kuusik, I. 1978, *Publ. Tartu. Astrophys. Obs.*, 46, 71
 Schmidt, M., & Green, R. F. 1983, *ApJ*, 269, 352
 Schweizer, F., Miller, B. M., Whitmore, B. C., & Fall, S. M. 1996, *AJ*, 112, 1839
 Shaw, M. A., Tzioumis, A. K., & Pedlar, A. 1992, *MNRAS*, 256, 6
 Smith, E. P., & Heckman, T. M. 1989, *ApJS*, 69, 365
 Soifer, B. T., et al. 1984, *ApJ*, 278, L71
 Sopp, H. M., & Alexander, P. 1991, *MNRAS*, 251, 112
 Stanghellini, C., O'Dea, C. P., Baum, S. A., & Laurikainen, E. 1993, *ApJS*, 88, 1
 Surace, J. A., et al. 1997, in preparation
 Taff, L. G., et al. 1990, *ApJ*, 353, L45
 Tremonti, C. A., Uomoto, A., Antonucci, R., Tsvetanov, Z., Ford, H. C., & Kriss, G. A. 1996, *BAAS*, 28, 1287
 Uomoto, A., Caganoff, S., Ford, H. C., Rosenblatt, E. I., Antonucci, R. R.,

- Evans, I. N., & Cohen, R. D. 1993, *AJ*, 105, 1308
van den Bergh, S. 1995, *Nature*, 374, 215
van den Bergh, S., Morbey, C., & Pazder, J. 1991, *ApJ*, 375, 594
Veilleux, S., Kim, D.-C., Sanders, D. B., Mazzarella, J. M., & Soifer, B. T.
1995, *ApJS*, 98, 171
Veilleux, S., Sanders, D. B., & Kim, D.-C. 1997, *ApJ*, 484, 92
Whitmore, B. 1996, *Photometry with the WFPC2* (Baltimore: STSCI)
Whitmore, B., & Schwiezer, F. 1995, *AJ*, 109, 960
Zhou, S., Wynn-Williams, C. G., & Sanders, D. B. 1993, *ApJ*, 409, 149

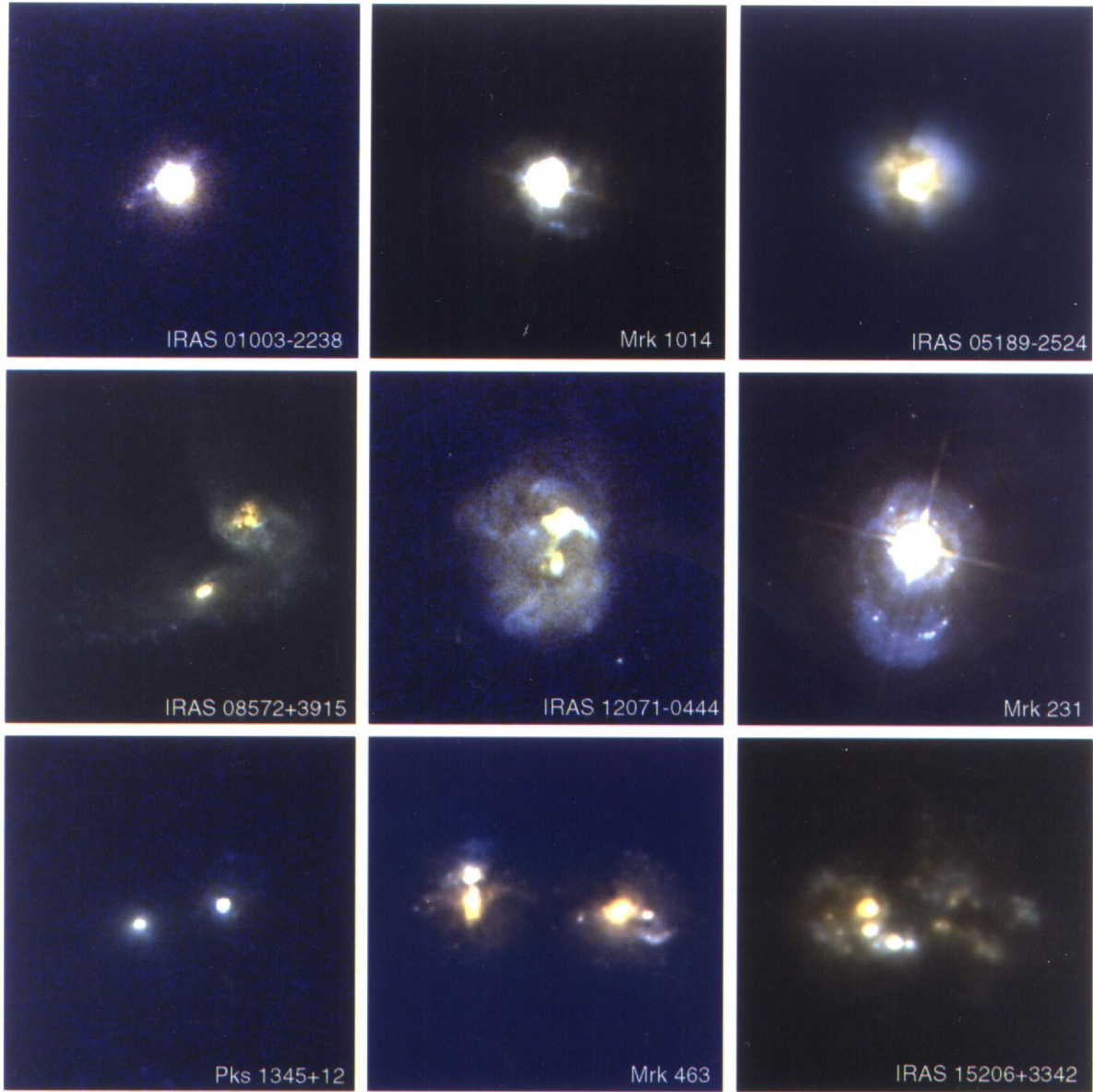


FIG. 3.—“Near-true-color” images of the nine warm ULIGs. The order and orientation are the same as in Fig. 1. For these images, we have linearly interpolated the galaxy SED and then presented it as a color image. The result should be similar to the actual color, as I is mapped to red, and B to blue. Both color and luminosity information are presented simultaneously. Note that the colors are *not absolute*, i.e., the color balance changes from image to image depending on the S/N in the different observations.

SURACE et al. (see 492, 119)